Universidade de Aveiro
2022

João Pedro Fidalgo Santos

Sensores híbridos baseados em fibras óticas de núcleo oco

Hybrid sensors based on hollow core optical fibers

Universidade de Aveiro
2022

João Pedro Fidalgo Santos

Sensores híbridos baseados em fibras óticas de núcleo oco

Hybrid sensors based on hollow core optical fibers

Dissertação apresentada à Universidade de Aveiro para cumprimento dos requisitos necessários à obtenção do grau de Mestre em Engenharia Física, realizada sob a orientação científica da Doutora Marta Sofia dos Anjos Ferreira, Investigadora Júnior do i3N e do Departamento de Física da Universidade de Aveiro.

o júri

Presidente	Professor Doutor Leonel Marques Vitorino Joaquim Professor Auxiliar do Departamento de Física da Universidade de Aveiro
Vogal – Arguente Principal	Doutor Manuel Filipe Pereira da Cunha Martins Costa Professor Auxiliar do Departamento de Física da Universidade do Minho
Vogal – Orientador	Doutora Marta Sofia dos Anjos Ferreira Investigadora Júnior do i3N e Departamento de Física da Universidade de Aveiro

agradecimentos / acknowledgments

Primeiramente, queria agradecer à minha orientadora, Doutora Marta Sofia dos Anjos Ferreira, por todo o auxílio, disponibilidade e conhecimento prestado ao longo deste trabalho. Acima de tudo, obrigado por me incentivar a ser curioso, e tentar coisas novas, independentemente do resultado previsto, e obrigado pela constante positividade e por realmente acreditar em mim, especialmente quando obstáculos foram encontrados.

Quero, ainda, agradecer ao projeto AROMA, financiado pelo FEDER, através do CENTRO2020 - Programa Operacional Regional do Centro, CENTRO-01-0145-FEDER-031568, e pelos fundos nacionais (OE), PTDC/EEI-EEE/31568/2017, UIDB/50025/2020 & UIDP/50025/2020, através da FCT/MCTES. Também agradeço à cooperação bilateral FCT/DAAD (FLOW, Project ID: 57518590) por possibilitar a visita aos laboratórios do Leibniz Institute of Photonic Technology (Leibniz-IPHT).

Ao Departamento de Física da Universidade de Aveiro, e ao i3N pelas condições oferecida e materiais cedidos que possibilitaram a realização deste trabalho.

Ao Leibniz-IPHT por facultar a fibra que foi utilizada mediante este trabalho.

Aos meus pais, pelo apoio incondicional e por toda a ajuda prestada.

A todos os colegas e amigos que estiveram do meu lado. Particularmente ao Noah e ao Kerem por toda a paciência, apoio e força transmitida ao longo destes anos, e especialmente nesta etapa. Dank je wel! Teşekkür ederim!

Palavras-chave

Fibras de núcleo oco, sensores em fibra ótica, sensores híbridos, tubo capilar de sílica, canal de acesso, fibra de núcleo oco quadrado, antirressonância, interferência de Fabry-Perot, interferência de Mach-Zehnder.

Resumo

Neste trabalho foram desenvolvidos vários sensores híbridos em fibra ótica baseados em fibras de núcleo oco. Num só elemento sensor foram excitados vários interferómetros que foram monitorizados para a medição simultânea de múltiplos parâmetros.

Primeiramente, um estudo foi desenvolvido sobre os interferómetros excitados numa secção de tubo de sílica fundida entre duas fibras monomodo. Foram explorados os interferómetros de Fabry-Perot (FP), propagação por antirressonância (AR), e de Mach-Zehnder (MZ).

O primeiro sensor híbrido desenvolvido foi baseado na fusão de um tubo capilar de sílica entre duas fibras monomodo onde se adicionaram canais de acesso através de dois métodos diferentes, tendo sido possível obter sensores com até dois canais de acesso. Foi feita a caracterização à pressão e temperatura de vários sensores com diferentes comprimentos onde se observam simultaneamente FP e AR. Foi feita uma proposta para medição simultânea dos dois parâmetros devido às diferentes sensibilidades dos interferómetros.

Uma outra configuração foi explorada onde o sensor foi curvado num formato balão, com o tubo capilar na posição superior central do mesmo balão. Num esquema em transmissão, um sensor com 1.2 cm num balão com 4 cm de comprimento apresentou AR e excitou um interferómetro de MZ forçado pela curvatura induzida pelo balão. A medição simultânea de deformação e temperatura foi obtida para a AR e MZ. Adicionalmente, foi criado um canal de acesso no capilar que permitiu deteção de pressão para ambos os interferómetros.

O último sensor desenvolvido foi baseado numa fibra de núcleo quadrado oco fundida entre uma fibra monomodo e um tubo capilar de sílica. Em reflexão, um sensor com 439 µm permitiu a excitação de três cavidades de FP distintas num só elemento sensor. Os vários modos foram monitorizados a vários parâmetros físicos através do método de filtros passa-banda de Fourier. O sensor foi proposto para medição simultânea de pressão, temperatura e curvatura, para uma certa rotação fixa.

Os dispositivos fabricados contendo apenas um elemento sensor revelaram possíveis aplicações como sensores híbridos para medição simultânea de vários parâmetros. Os sensores possuem tamanho reduzido e alta robustez, juntamente com configurações simples, tornando-os excelentes candidatos para a sua implementação em várias aplicações.

Keywords

Hollow core fiber, optical fiber sensors, hybrid sensors, silica capillary tube, access channel, hollow square core fiber, antiresonance, Fabry-Perot interference, Mach-Zehnder interference.

Abstract

In this work, the development of several hybrid optical fiber sensors based on hollow core fibers was aimed. The sensing structures enhanced multiple interferometers in a single sensing cavity, which were monitored towards simultaneous measurement of multiple parameters.

Firstly, a study was carried out over the different interferometers that arise in a section of silica capillary tube (SCT) spliced between two single mode fibers (SMF). The Fabry-Perot interferometer (FPI), antiresonant guidance (AR) and the Mach-Zehnder interferometer (MZI) were explored.

The first hybrid sensor fabricated was based on the SMF-SCT-SMF structure with access channels instilled on the fiber with two methods that allowed the fabrication of an up to two-access channel sensor. The sensor was characterized to pressure and temperature in a reflection scheme, enhancing an FPI and AR for a 2 mm sensor. Different sensitivities were attained for both interferometers, thus the simultaneous measurement of the parameters under study was proposed.

A different explored configuration was the balloon-like fiber sensor with the SMF-SCT-SMF configuration. This structure was bent in a balloon shape with the SCT in the top-center position. The 1.2 cm SCT length sensor was studied in a transmission configuration with a 4 cm balloon-length, enhancing AR guidance as well as an MZI, which was enforced by the bending derived from the balloon structure. Simultaneous measurement of displacement and temperature was achieved for the MZI and AR. Additionally, an access channel was instilled in the SCT, and the balloon-like sensor was sensitive to pressure for both components.

Finally, a configuration based on a SMF-hollow square core fiber-SCT was developed and studied in a reflection scheme. A 439 µm long hollow square core fiber was able to excite three distinct FP cavities in a single sensing element. The different modes were monitored towards several physical parameters by using the Fourier band-pass filter method. The sensor was able to achieve a multiparameter simultaneous measurement of pressure, temperature, and curvature, for a certain fixed rotation.

All the studied inline sensors all revealed potential hybrid application for simultaneous measurement of several parameters while constituting a single sensing head. The sensors possess reduced dimensions, high robustness, and simple configurations, making them great contenders for their implementation on several applications.

Table of Contents

List of Figures

Acronyms

AR	Antiresonance
ARROW	Antiresonant reflecting optical waveguide
FBG	Fiber Bragg grating
FBPF	Fourier band-pass filter
FCF	Four core fiber
FFT	Fast Fourier transform
FMF	Few-modes fiber
FP	Fabry-Perot
FPI	Fabry-Perot interferometer
FSR	Free spectral range
HB	Highly birefringent
HCF	Hollow core fiber
HSCF	Hollow square core fiber
LPG	Long period grating
MFD	Mode field diameter
MI	Michelson interferometer
MMF	Multimode fiber
MMI	Multimode interferometer
MOF	Microstructured optical fiber
MZI	Mach-Zehnder interferometer
NCF	No-core fiber
OFS	Optical fiber sensor
OSA	Optical spectrum analyzer
PCF	Photonic crystal fiber
PMF	Polarization maintaining fiber
RI	Refractive index
RH	Relative humidity
SCT	Silica capillary tube
SI	Sagnac interferometer
SMF	Single mode fiber
TEC	Thermal expansion coefficient
TIR	Total internal reflection
TOC	Thermo-optic coefficient

List of Symbols

C	Curvature
d	Thickness of the FP resonator
d_b	Balloon bending diameter
D	Distance between the fixed stage and translation stage
E_1	Reflecting antiresonant light beam
E_2	Reflecting resonant light beam
FSR_{AR}	Free spectral range of the AR guidance
FSR_{FPI}	Free spectral range of the FPI
FSR_{MZI}	Free spectral range of the MZI
h	Height of the bending
k	Wavenumber
L	Length of the sensor
L_b	Balloon length
L_c	Critical length
M	Interface mirror
m	Resonance order
$n(x)$	RI profile when straight
$n'(x)$	RI profile when bent
n_0	Refractive index of air
n_1	Refractive index of SMF core
n_2	Reflective index of silica
n_{eff}	Effective RI
P	Pressure
r	SCT inner radius
r_b	Balloon bending radius
R	Bending radius
R^2_{FPI}	Linearity coefficient of FPI response
R^2_{AR}	Linearity coefficient of AR response
T	Temperature
w	Thickness
α	Thermal expansion coefficient
β	Thermo-optic coefficient
δ	Phase difference
ΔC	Variation of curvature
ΔD	Variation of displacement
ΔP	Variation of pressure
ΔT	Variation of temperature
Δn	Effective RI difference
$\Delta\lambda$	Mean wavelength shift
$\Delta\lambda_{AR}$	AR wavelength shift
$\Delta\lambda_{FPI}$	FPI wavelength shift
$\Delta\lambda_{MZI}$	MZI wavelength shift
θ_i	Incident FPI angle
θ_j	Incident AR angle
θ_t	Propagation phase variation
κ_i^j	Sensitivity of the i interferometer to the j measurand
$\kappa_{C,i}$	Filter sensitivity to curvature, where i is the filter 1, 2 or 3
$\kappa_{P,i}$	Filter sensitivity to pressure, where i is the filter 1, 2 or 3
$\kappa_{T,i}$	Filter sensitivity to temperature, where i is the filter 1, 2 or 3

Λ	Optical path difference
λ	Wavelength
λ_m^{AR}	Interference wavelength of AR
λ_m^{FPI}	Interference wavelength of FPI
λ_m^{MZI}	Interference wavelength of MZI
σ	Standard deviation

1. Introduction

1.1 Overview

One of the highlights in the optical field that begun in the 20th century was the development of optical fibers. The transmission of light based on the total internal reflection (TIR) effect, which constitutes a guided mechanism within a restricted medium, had already been developed in 1854 [1]. The knowledge that light could propagate in a material when the right conditions are met ignited the scientific community to realize the incredible potential for major applications, specifically in the communication field. Firstly, optical glass fibers were made as successful waveguides that could transmit light with some effectiveness. However, their high losses prevented the fulfillment beyond medical applications [2].

As low attenuation was clearly a goal to achieve, scientists started to explore optical fibers in other fields, including optical communications, with a successful low loss fiber developed in 1966 by Charles Kao, leaning on the high purity of silica as a way to decrease attenuation [1,3]. These discoveries were a true breakthrough, particularly in the telecommunication area with ever-decreasing bandwidth cost, but also in the sensing field, undergoing tremendous advancements over the following decades. In the context of this work, the sensing field of optical fibers shall be of greater focus.

Before optical fiber sensors (OFS) had their revolution in the scientific community, electronic sensors had already been developed, with their usage being continuously and extensively explored for numerous applications. However, OFS became immensely noticed when their notorious advantages were thoroughly understood, namely immunity to electromagnetic interferences as well as their small dimensions and weight, high flexibility, and high reliability [3,4]. These sensors can be implemented in situations of high adversity whereupon electronic sensors would fail to perform. The aforementioned advantages, together with resistance to corrosion, low losses, and ability to be multiplexed facilitated the use of OFS as alternatives to electronic and chemical sensors [5,6]. The continuous development of sensing configurations aims for the achievement of a quality optical sensor that possesses high sensitivity, selectivity, high measurement accuracy, fast response time, and reproducibility [7].

Among the most dissimilar fiber configurations developed as innovative waveguide propagations for light manipulation, the capillary tube is one to highlight. Capillaries are cylindrical fiber structures that possess a hollow core which is surrounded by a cladding material with a higher refractive index (RI). The capillary tube is described as a leaky waveguide, which was first used in a hollow core fiber in 1986 [8]. Due to the leaky waveguide propagation in capillaries, one of the phenomena that can occur with the rightfully enhancing configuration is the antiresonant reflecting optical waveguide, first introduced in the same year for SiO_2-Si multilayer structures [9]. Although capillaries had already seen usage in other applications, it was only in 1993 that capillaries were applied as a waveguide [10]. A year later, this configuration was employed for a sensing purpose for the first time [11,12].

Another interesting class of fibers is the microstructured optical fiber (MOF), or photonic crystal fiber (PCF), first developed in 1996 with a creation of a solid central core fiber surrounded by air channels [13]. These fibers can present a solid core or a hollow core, allowing for different light guidance mechanisms. The PCF waveguide is characterized by having periodic arrangements of air holes disposed along the fiber length that are centered on a hollow or solid core [13].

These fibers soon attracted the attention of the scientific community due to their ability to function as unique waveguides, possessing low attenuation and dispersion over broad bandwidth as well as the ability to manipulate certain optical properties of light, such as nonlinearities, birefringence, among others [14,15]. Not only did they reveal potential for low loss communication, but it also garnered interest for many sensing applications. The increasing investments in these unique fibers sparked an enhancement in the sensing field, thereupon realizing the yearning for the development of new fiber geometries able to manipulate other intrinsic optical properties.

A variety of OFS designs with different mechanisms and configurations can modulate light for the monitoring of several physical, chemical, and biological parameters. These devices allow for the detection of a property change of the propagating light, a consequence of fluctuations occurring in the external environment. The working principle of OFS is typically based on light interference or resorting to fiber gratings, such as fiber Bragg gratings (FBGs) or long period gratings (LPGs), though other mechanisms can also be used, such as distributed sensors [16]. Among the interference-based sensors, one would draw attention to the Fabry-Perot interference (FPI), Mach-Zehnder interference (MZI), the Michelson interference (MI), the Sagnac interference (SI), the multimode interference (MMI), and the interference based on the antiresonant (AR) guidance. The different types of fiber sensors are liable to perform spatially resolved measurements. More specifically, interferometric sensors are more suitable for single-point detection, whilst gratings and distributed sensors showcase quasi-distributed and distributed measurements, respectively. Such variety of mechanisms enables a large potential of measurands and applications, further corroborating the versatility of OFS [16].

1.2 Motivation and objectives

The manifold types of fibers that can be arranged in a near infinite number of configurations is enticing towards unraveling the true potential of OFS, and truly pushing the boundaries of the applicability of light manipulation. Though countless OFS have been extensively explored and reported, the development of hybrid sensors, wherein multiparameter detection is possible, remains an entirely incomplete endeavor.

The ability to measure two or more parameters simultaneously and independently with good performance is an irrefutable advantage that offers great attractiveness of hybrid sensors in detriment of conventional OFS. In literature, proposed sensors that detect various parameters usually pertain a hindrance related with the dependence of one parameter with another. The most common example is the measurement of RI and pressure, both of whom highly depend on the temperature of the system [17]. To compensate for cross-sensitivity, typically another cascaded sensor is added that is established outside of the measurement system or by adding another sensor that is temperature insensitive. This results, for both solutions, in an increase of system complexity and total sensing length. Another approach consists in adopting hybrid sensors, in which a single structure can independently and simultaneously measure multiple parameters, resulting in a miniaturization of the sensor, presenting simpler configurations with unequivocal working principles and unpretentious fabrication techniques, bearing an elegance in the sensing field.

Heretofore, scarce amount of OFS have demonstrated multiparameter detection with independent and simultaneous measurements of more than two measurands. Moreover, to accomplish this goal, ofttimes cascaded elements are introduced. With this, the objectives of this work are settled into the fabrication and characterization of novel, compact size fiber sensors that possess only one sensing head and can be applied as hybrid sensors for simultaneous measurement of multiple parameters.

The sensors will be based on hollow core fibers, fabricated at the Leibniz Institute of Photonic Technology (Leibniz-IPHT) in Germany, as inline sensing structures. The first main objective is to develop novel configurations of a hybrid sensor based on a silica capillary tube (SCT) with new configurations for the measurement of physical parameters, namely pressure, temperature, and displacement. The second main objective is to evaluate the response to physical measurands of a hollow square core fiber (HSCF) as a sensor in a reflection scheme, by monitoring the interferometric phenomena that are enhanced in the sensor, exploring a multiparameter sensor application that can achieve simultaneous detection of pressure, temperature, and curvature.

1.3 Main contributions

João P. Santos, J. Bierlich, J. Kobelke, M.S. Ferreira, "Simultaneous measurement of displacement and temperature using balloon-like hybrid fiber sensor", *Optics Letters*, 47(15) 3708-3711, 2022.

João P. Santos, J. Bierlich, J. Kobelke, M.S. Ferreira, "Hybrid fiber sensor based on capillary tubes for simultaneous measurement of pressure and temperature", *Iberic Meeting of Optics Students*, 2022 [Oral presentation].

João P. Santos, J. Bierlich, J. Kobelke, M.S. Ferreira, "Capillary based hybrid fiber sensor in a balloon-like shape for simultaneous measurement of displacement and temperature", *V International Conference on Applications of Optics and Photonics*, 2022 [Oral presentation].

1.4 Thesis outlook

This thesis is divided in seven chapters, in which different hybrid fiber sensors are studied. In the first chapter, an overview of optical fibers is presented, exploring with greater focus the SCT and the PCF and their usages as optical fiber sensors. A brief motivation regarding the use of hybrid fiber sensors is also presented. The objectives are stated, and main contributions are identified.

In the second chapter, a state-of-the-art is presented for different types of multiparameter fiber sensors regarding their configuration and working principle, particularly those developed in the past 5 years.

In the third chapter, a theoretical description of the SCT in a sandwich structure is provided regarding its guidance mechanisms. A theoretical and simulation analysis is also done on the subject of the possibly enhanced interferometers in the fiber configurations explored in this work.

In the fourth chapter, an experimental procedure is established for the development and characterization of access channel based capillary fiber sensors, presenting the spectral results and responses to pressure and temperature.

In the fifth chapter, a balloon-like fiber sensor based on a SCT is explored, in a transmission scheme, for pressure, displacement, and temperature measurements.

In the sixth chapter, a characterization of the HSCF is performed in a reflection configuration for multiple parameters, namely pressure, temperature, strain, and curvature.

In the seventh and final chapter, some final remarks are given, and future work suggestions are presented.

2. State-of-the-art

The state-of-the-art of this thesis is based on a revision of scientific articles with focus on similar configurations that align with those developed in this work. It will focus on multiparameter hybrid fiber sensors, with respect to their sensing mechanisms, namely interference- and grating-based fiber sensors, employed structure as well as the parameters detected. The main characteristics of the sensors will, also, be highlighted, such as the attained sensitivity, resolution, and length.

In order to distinguish multiple parameters in a single-point measurement, low cross-sensitivity is required. This becomes even more pronounced in scenarios that require higher accuracy and/or greater resolution, thus the development of fiber sensors that can measure more than one parameter independently and simultaneously is incredibly favorable. Since most sensors that detect various parameters usually present sensitivity to temperature, cascaded structures are frequently employed to overcome cross-sensitivity issues in the sensor.

In regards to designs and principles of operation of multiparameter sensors one would emphasize the stacking of FPIs; MZI and in-fiber MI; FBGs and LPGs; antiresonant reflecting optical waveguide (ARROW) and a combination of FPIs, MZIs and gratings in a cascaded structure.

It was found that the most common measurands for hybrid measurements are the RI and temperature followed by strain or some form of fiber deformation. Concerning the combinations employed for multiparameter detection, the most common were found to be an MZI cascaded with a grating with the second most common being an FPI cascaded with a grating.

2.1 Hybrid sensors based on FPIs

The stacking of multiple FPIs with low finesse and different cavity lengths between one another results in a spectrum with multiple harmonic oscillations, that is, with nearby frequencies which can be separated with fast Fourier transform (FFT) band-pass filters. The independent measurement of temperature and pressure is frequently achieved with two cascaded FPIs that are selectively sensitive to either parameter [18]. The most common design for this purpose utilizes a fiber-tip structure, where the first FPI is constituted by a waveguide that is temperature-dependent and the second FPI is used as the sensing cavity. The temperature sensitive FPI can be composed of a section of an SMF fiber placed between two reflective mirrors that is adjacent to the pressure sensing cavity. The latter can be constituted by a micromachined cavity on its tip. The pressure sensitivity is achieved by thinning the short-spliced fiber segment to form a flexible diaphragm, which can be done with chemical etching [19] or through femtosecond micromachining [18].

Another pressure sensing method can be achieved by modifying the RI of an open path FPI air cavity with the entrance of gas in the cavity, as RI is correlated to pressure, eliminating the necessity of a diaphragm, and its complications. The simultaneous measurement of pressure and RI was achieved with two stacked FPIs with the first constituting an open cavity for RI detection and the second FPI is an air cavity with a silica diaphragm for pressure sensing, as shown in Figure 2.1a [20]. Other parameters can be detected with this design, including strain and temperature. For this purpose, a short open-air cavity was spliced between two SMFs, where the second SMF is a short section as depicted in Figure 2.1b [21].

Temperature and RI detection was attained in a combination of an all-silica FPI that is sensitive to temperature and an open micro-cell sensitive to RI with a maximum RI resolution of 5×10^{-9} RIU [22]. In 2020, a multiparameter sensor based on a very short HCF segment, with a micromachined micro-

hole, spliced between SMFs, was developed [23]. The open cavity can detect air pressure, RI, and temperature while the short section of SMF is only sensitive to temperature. In a reflection scheme, the sensor attained the highest sensitivities of 3.98 nm/MPa, 1116 nm/RIU, and 185.6 pm/°C to pressure, RI, and temperature, respectively with resolutions of 0.012 MPa, 10^{-5} RIU and 0.08 °C.

Finally, a stack of multiple FPIs was described to measure up to four parameters simultaneously: thermal conductivity, pressure, RI, and temperature, as seen in Figure 2.1c [24]. This was accomplished by cascading three FPIs, with the first being a silica capillary and a diaphragm for pressure detection, the second, a U-shaped open silica micro-cell for RI sensing, and the third, a section of vanadium-doped fiber. The latter cavity measures temperature and thermal conductivity by active laser heating, resulting in selective short wavelength absorption while being transparent to longer wavelengths. The heating power changes the segment temperature, allowing for thermal conductivity detection of the surrounding fluid. The obtained resolutions were 2×10^{-3} °C, 10^{-4} MPa, and 5×10^{-7} RIU for temperature, pressure, and RI, with a thermal conductivity sensitivity of 10^{-3} W/mK.

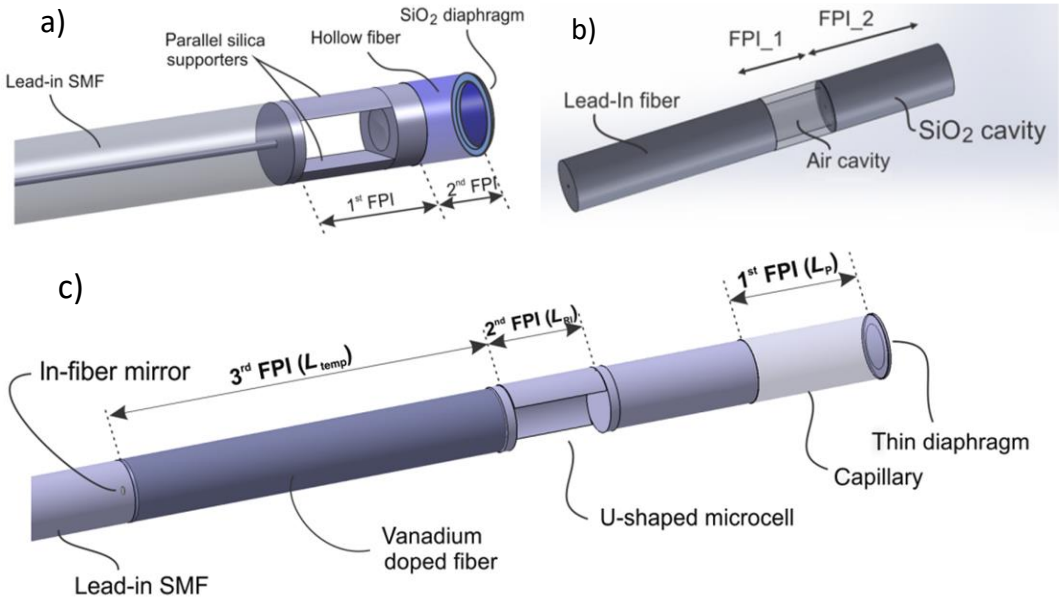

Figure 2.1: (a) Pressure-RI sensor design [20]. (b) Strain and temperature sensor design [21]. (c) Thermal conductivity, pressure, RI, and temperature hybrid sensor [24].

2.2 Hybrid sensors based on MZIs

The mode interference between a fundamental and a higher order or a cladding mode is a frequently employed interference mechanism. Usually, MZIs are used as RI and temperature sensors. When cascading two MZIs for temperature and RI detection, each interferometer can be used to measure one of the parameters. For instance, a short section of MMF spliced between two SMFs is temperature sensitive (9.2 pm/°C) while a cascaded abrupt short taper made of SMF is RI sensitive (113.66 nm/RIU), as illustrated in Figure 2.2a [25]. Moreover, a SMF- no-core fiber (NCF) -SMF-MMF-SMF structure can be used as a RI-temperature sensitive interferometer pair [26]. This design can also be used for strain and temperature detection, by having cascaded MZIs that yield different sensitivities to these parameters, for example, in a SMF-MMF1-MMF2-SMF configuration shown in Figure 2.2b, with demonstrated sensitivities of 0.35 pm/με and 11.16 pm/°C, for strain and temperature, respectively [27].

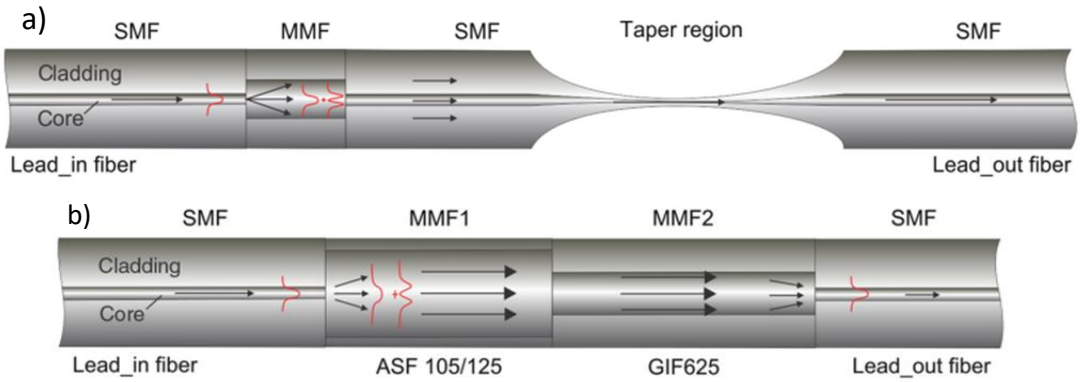

Figure 2.2: (a) Temperature and RI sensor based on SMF-MMF-SMF elongated with a taper region [25]. (b) Strain and temperature sensor based on splicing fibers with dissimilar mode fields [27].

Three-parameter (RI, strain, and temperature) sensors were proposed, including a bend-insensitive fiber with a pair of abrupt tapers, forming an MZI with inner and outer cladding modes that can perform temperature and axial strain compensated RI measurements [28]. Additionally, a down taper was introduced between two adjacent up tapers in an SMF that can perform simultaneous measurement of these three parameters [29]. Maximum sensitivities of 132 nm/RIU, 0.7 pm/με, and 90.6 pm/°C were obtained for RI, strain, and temperature, respectively.

A multiparameter sensor based on a NCF combined with a few-mode fiber (FMF) was demonstrated, where the three transmission resonance peaks can measure RI, strain, and temperature [30]. In a different configuration of cascaded SMF-NCF-FMF-NCF-SMF with a sensing length of ~4 cm, the NCF is the input and output coupler for the MZI which has three interference dips that can simultaneously measure two measurand-pairs: temperature and relative humidity (RH), and temperature and RI [31]. The highest attained sensitivities for this sensor were 0.095 nm/°C, 0.034 nm/%, and 134 nm/RIU.

2.3 Hybrid sensors based on MZIs cascaded with FPIs

The possibility of cascading structures brings about the combination of different interferometer for hybrid measurements. Their analysis is facilitated due to the distinct spectral responses of each interferometer. A design involved a temperature detecting FPI cavity filled with alcohol (0.454 nm/°C), and the RI sensing was performed via an MZI resultant from an SMF-HCF-PCF-SMF structure (178.7 nm/RIU) [32].

A different structure relied on a section of SMF spliced between an air bubble and a thin taper, to detect RI variations (-103 nm/RIU) whilst temperature detection was performed by an MZI modulation (103.2 pm/°C), combined with an FPI that could measure transverse load (1.596 nm/N) [33]. In 2022, a RI insensitive, strain and temperature sensor was developed with an SMF-HCF-FMF-SMF design of ~5 cm length where the FMF-SMF splice has an offset, thus forming an MZI while the HCF and the two interfaces form an FP cavity [34]. The maximum sensitivities attained were 5.89 pm/με and -38.8 pm/°C for strain and temperature, respectively.

2.4 Hybrid sensors based on FBGs and LPGs

Typically, conventional FBGs can detect mechanical strain and temperature, while LPGs can be used to couple multiple guided modes and are sensitive to RI. A dual-parameter sensor involved two FBGs inscribed in fibers with different cladding diameters, as shown in Figure 2.3. The FBGs had equal

temperature sensitivities but different strain responses with an attained resolution of 5.3 με and 0.6 °C for strain and temperature, respectively [35].

Figure 2.3: Strain and temperature sensor based on FBGs [35].

The simultaneous detection of pressure and temperature has also been done with FBGs, namely with a pair of gratings, one inscribed in an SMF and the other in a pressure-sensitive MOF [36]. A novel approach was proposed based on gratings for three-parameter sensing that is constituted by an LPG written in a polarization-maintaining Panda fiber, able to measure surrounding RI, temperature, and strain, with the maximum sensitivities attained of -12 nm/RIU, 79 pm/°C, and -2.2 pm/με, respectively [37].

2.5 Hybrid sensors based on gratings cascaded with FPIs and MZIs/MIs

The cascading of a grating with FPIs brings about a large window of application possibilities towards multiparameter sensing. For instance, an SCT was spliced between two SMFs to create an FPI cavity, which was cascaded with an FBG for strain and temperature detection [38].

In another example, an SMF-PCF-SMF design where the PCF is in-between SMFs containing FBGs, can provide simultaneous pressure – by the compression of the PCF – and temperature – by the FBG wavelength shift – measurements [39]. In 2019, a multiparameter sensor based on an SMF and UV curable adhesive was demonstrated for two pairs of dual-parameter detection: gas temperature and pressure, and liquid RI and temperature. The 1-mm-long-sensor consists of three FPIs resulting from the integration of the UV glue and a segment of SMF with an inscribed FBG [40].

Analogously, MZIs have been utilized with gratings to achieve multiparameter sensing predominantly for RI and temperature detection. One would highlight a unique design depicted in Figure 2.4 of a strongly bent SMF fiber section containing an FBG that forces light to couple into the cladding, interfering with the core mode, thus providing RI sensitivity (maximum 166 nm/RIU) while the FBG provides the temperature compensation (31.7 pm/°C) [41].

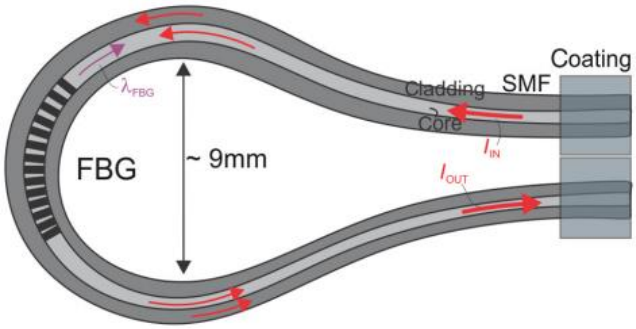

Figure 2.4: RI and temperature sensor based on a strongly bent FBG inscribed in an SMF [41].

Moreover, a three-parameter sensor for strain, RI, and temperature was developed with 3 sensing regions with a total length of 27 cm: an FBG inscribed in an SMF (strain and temperature sensitive); an FBG inscribed in a tapered SMF section (sensitive to all parameters); and a coreless fiber spliced between two SMFs, defining an MZI (also sensitive to all parameters) as shown in Figure 2.5a [42]. The highest sensitivities attained were 5.77 pm/με, 116.5 nm/RIU, and 34.82 pm/°C for strain, RI, and temperature, respectively. In 2020, a RI, temperature, and curvature sensor was proposed with a

splicing point tapered FBG + SMF- four-core fiber (FCF) -SMF structure forming two waste-enlarged tapers on the splices between the FCF and the SMFs that result in an MZI. The latter gives RI and curvature measurements with sensitivities of 116.4 nm/RIU and 15.6 pm/m^{-1}, respectively, with FBG compensating for temperature showcasing a sensitivity of 67.3 pm/°C [43].

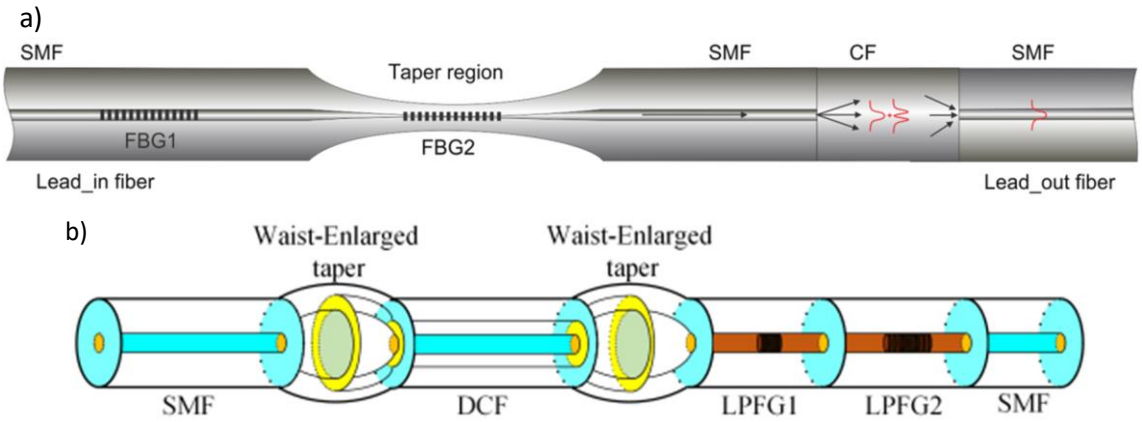

Figure 2.5: Strain, RI, and temperature sensor based on (a) FBG inscribed in an SMF and a taper, cascaded with SMF-CF-SMF structure [43]. (b) SMF-DCF-SMF structure with waist-enlarged taper splices cascaded with two LPGs [44].

Additionally, a three-parameter sensor was developed that is composed by a FCF spliced between two SMFs, one of whom had an inscribed FBG. The monitoring of the FBG resonance and two transmission dips made simultaneous measurement of RI, strain, and temperature viable with resolutions of 0.0004 RIU, 11.06 με, and 0.17 °C, respectively [45].

More recently this year, a design was proposed of a 2.4-cm-long dumbbell-shaped double-cladding fiber spliced between SMFs to form a waist-enlarger taper and two cascaded LPGs as shown in Figure 2.5b. Simultaneous detection of temperature, RI, and axial strain was reported, with maximum sensitivities of 89.8 pm/°C, −141 nm/RIU, and −3.14 pm/με, respectively [44].

2.6 Hybrid sensors based on the ARROW mechanism

Another interesting principle for optical fiber sensors is the ARROW mechanism, particularly of HCF, as their interior can be filled with various fluids and their external cladding can be coated with functional films [17].

A double layer AR structure with 8 cm length was achieved by inserting a small diameter HCF in a large diameter polymethyl methacrylate HCF, with sensitivity to tensile strain of 28 pm/με and low temperature cross-sensitivity (1.67 pm/°C) [46]. A gas pressure antiresonant sensor was developed based on an SMF-HCF-SMF design of 5 mm where the HCF has an open microchannel created by femtosecond laser drilling [47]. An enhanced configuration with a 1 mm length shown in Figure 2.6a involved an additional FPI formed in the HCF along the axial direction, achieving simultaneous pressure and temperature measurements with sensitivities of 3.9 nm/MPa at 37 °C and ~0.58 nm/°C, respectively [48].

For curvature and temperature detection, a HCF was spliced between two SMFs with tapers on both splices which excites an ARROW and an MZI. The latter is highly sensitive to temperature (70.7 pm/°C) while ARROW is sensitive to curvature in intensity [49]. A design with 5.2 cm composed of an SMF-MMF-HCF-SMF excited an MMI as well as an AR effect that can detect curvature and temperature [50].

A hybrid sensor based on an SMF-HCF-SMF design was able to enhance an FPI and an AR guidance that can achieve simultaneous strain and temperature measurements with sensitivities of 2 pm/με and 21.11 pm/°C, respectively [51]. A dual-parameter sensor was proposed based on a quartz capillary with an open cavity and a sphere cavity that is able to detect pressure and temperature with highest attained sensitivities of 4.278 nm/MPa and 6.8 pm/°C [52]. A sensor based on an SMF-HSCF-SMF configuration was developed for multiparameter sensing. The few-millimeter-long sensor can enhance external and internal AR, as well as an MZI and a cladding mode interference, as is depicted in Figure 2.6b. It was able to measure curvature and temperature through the double antiresonances [53], detect temperature independent RI [54] and perform a strain, curvature, and temperature measurement using the 3 mechanisms [55].

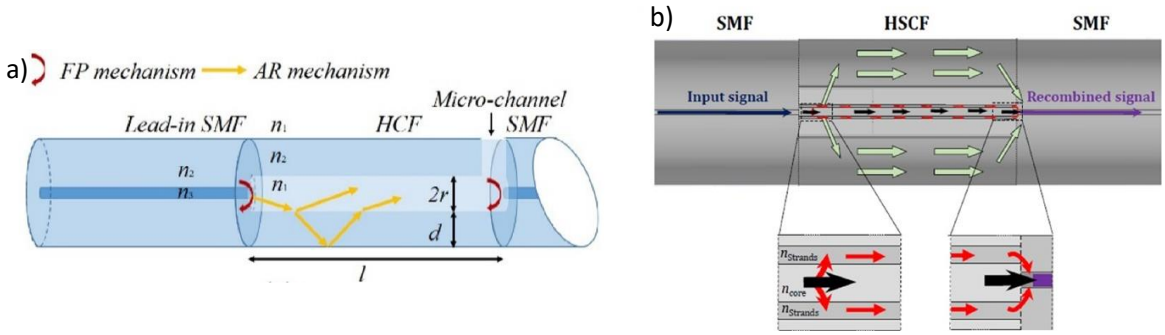

Figure 2.6: (a) Pressure and temperature SMF-HCF-SMF sensor [48] . (b) Scheme of the SMF-HSCF-SMF structure with the different interferometric paths represented by arrows [54].

A three-parameter hybrid fiber sensor was made by splicing a section of HCF between an air bubble and an up-taper, where the air bubble acts as an FPI and serves the enhancement of an MZI while the HCF is used as an ARROW. The FPI was found to be sensitive to transverse load, while the MZI detected temperature, and the ARROW measured curvature [56].

In Table 2.1, a list of multiparameter sensors developed in the last 5 years is provided with a description of their respective configurations and principles, together with combinations of detectable parameters. One would highlight the frequent employment of cascaded structures as well as the combination of an(some) interferometer(s) with gratings. Furthermore, the number of multiparameter (3+) sensors is rather diminutive when compared with simple or hybrid OFS, as combining more than two parameters represents a significant challenge. The requirement of advanced interrogation equipment as well as complex, and expensive, fabrication methods raise the question of how to develop a compact size, economic and simple multiparameter fiber sensor. This matter, thus, comes about as an intricate subject, propitious to spark new configurations and remains an object of study by the scientific community that is far from being completed.

Table 2.1: Figures of merit of some multiparameter (3+) OFS within the last 5 years and their corresponding structures, measurands and designs, based on SMF, HCF, gratings and other structures. The acquisition scheme can be either in reflection (R) and/or in transmission (T).

Year	Structure device[a]	Sensor principle	Measurand	Sensitivity	Type	Ref
2018	Up-down-up taper in SMF	MMI	RI Strain Temperature	132 nm/RIU 0.7 pm/με 90.6 pm/°C	T	[29]
2019	SMF + FBG – UV glue – SMF	FBG + 3 FPIs	Pressure + Temperature/ RI + Temperature	8.45 nm/MPa 748 pm/°C 156.8 nm/RIU	R	[40]
2019	LPG + Panda fiber	Mode coupling	RI Strain Temperature	-25 nm/RIU -2.2 pm/με 79.1 pm/°C	T	[37]
2019	NCF – FMF	MZI	RI Strain Temperature	97 pm/RIU -4.1 pm/με 194 pm/°C	T	[30]
2020	Air bubble – HCF – up-taper	FPI + MZI + ARROW	Transverse load Curvature Temperature	1.53 nm/N 33.2 dB/m^{-1} 20.3 pm/°C	R+T	[56]
2020	FBG – SMF + taper – FCF – SMF + taper	Bragg reflection + MZI	RI Curvature Temperature	116.4 nm/RIU 15.6 pm/m^{-1} 67.3 pm/°C	T	[43]
2020	SMF – HCF + micro-hole – SMF	FPIs	Pressure RI Temperature	3.98 nm/MPa 1116 nm/RIU 185.6 pm/°C	R	[23]
2021	Air bubble – SMF – thin taper	FPI + MZI	Transverse load RI Temperature	1.596 nm/N -103 nm/RIU 103.2 pm/°C	R+T	[33]
2022	SMF – NCF – FMF – NCF – SMF	MZI	Temperature + Humidity/ Temperature + RI	0.095 nm/°C 0.034 nm/% 134 nm/RIU	T	[31]
2022	SMF + taper – Double-cladding fiber – taper + 2 LPGs	MZI + mode coupling	Temperature RI Axial strain	89.8 pm/°C -141 nm/RIU -3.14 pm/με	T	[44]
2022	SMF – HCF – FMF – (offset)SMF	FPI + MZI	RI Strain Temperature	Insensitive 5.89 pm/με -38.8 pm/°C	R+T	[34]
2022	SMF – HSCF – SMF	ARROW + MZI + MMI	Curvature Strain Temperature	-2.21 nm/m^{-1} -2.72 pm/με 32.8 pm/°C	T	[55]

[a]A " – " indicates a splice while a "+" represents a cascaded structure.

3. Working principle

3.1 Introduction

The search for new waveguides with specific optical properties was contributory to a huge development of optical fibers. A conventional optical waveguide is defined by light confined inside a region with a RI that is higher than the surrounding medium. For standard fibers that would correspond to its core and cladding, respectively. In this type of fibers, the total internal reflection mechanism is evidenced [2].

There is, also, a class of optical waveguides in which the core RI is lower than that of the cladding. These optical waveguides are described as leaky waveguides where guided modes are realized with low loss when surrounding the core with highly reflective claddings, achieving a RI profile that uses the antiresonant waveguide to provide a transverse confinement of the light in the core [57].

Among hollow core fibers, one of its simplest structures is the SCT, characterized by a silica cladding and a hollow core. The light confinement mechanism of this type of fiber is, indeed, described as a leaky waveguide [8]. This waveguide meets the antiresonant guidance criteria, whose interferometric phenomenon is based on the coupling of light into the cladding, for resonant wavelength, and the reflection of light into the core, for antiresonant wavelengths. Different capillary dimensions as well as dissimilar configurations can enhance distinct interferometers [58] which will constitute the sensing principle of the fiber sensors.

3.2 Operation mechanisms

In order to illustrate the studied interferometers, a configuration that was used for the better part of this work will be explored as an exemplary tool. This configuration is comprised of a section of SCT spliced between two SMFs, as seen in Figure 3.1. The length of the capillary, *L*, and its inner diameter, *2r*, have a direct influence on the resulting interferometer, even determining whether the phenomenon is present or not. The RIs of the silica cladding and hollow core are denoted n_2 and n_0, respectively, while the RIs of the SMF core and cladding are designated as n_1 and n_2, respectively. At 1550 nm, the RIs are approximately $n_0 = 1; n_1 = 1.445; n_2 = 1.444$ [48,59].

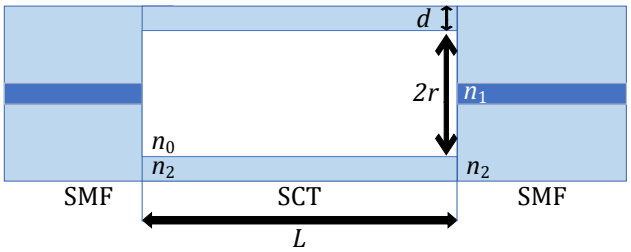

Figure 3.1: Schematic diagram of the SMF-SCT-SMF configuration.

The leaky waveguide established in the capillary allows for light to travel through the core as well as through the cladding when specific conditions are met. The propagation of light in these distinct regions may also allow for a set of interferometric phenomena to occur. The interference of light is based on the superimposing of two or more light beams that possess the same frequency and showcase a phase difference. The latter is usually originated due to the difference of optical paths in light guidance, leading to constructive and destructive interferences that create a pattern. In the forenamed sandwich configuration, there are four interference phenomena that can occur, namely the FPI, AR, MZI and MMI, of which the first three will be explored in this work. These mechanisms

are sensitive to the surrounding medium, making this type of fiber an excellent candidate for sensing purposes. The following section will briefly discuss the physical properties of the studied interferometers that can be enhanced in the SCT.

3.2.1 Fabry-Perot interferometer

Generally, the FP interferometry occurs when two high reflectance parallel surfaces are placed a certain distance, *L*, from one another, with air constituting the FP cavity between the interfaces. Towards a sensing tool application, the FP interferometer is described as extrinsic when the cavity that functions as a sensing element is located outside of the fiber whereat guided light is modulated by an external device. An example of this interferometer can be given by two fiber tips, defining a mirror on each free end, that are brought close enough to enhance interference. On the other hand, an intrinsic FP interferometer is attained when the FP cavity located inside the optical fiber, which is the example of the hollow core fiber spliced between two SMFs [18,60].

When light travels towards the cavity with a near normal incidence ($\theta_i \approx 0°$), multiple reflections will occur that can interfere with one another, thus creating a multiple light beam interferometer [48]. For the configuration at hand, it can be seen in Figure 3.2 that the interfaces correspond to the mirrors M_1 and M_2 defined by the two SMF-capillary interfaces, and the FPI is formed along the axial direction.

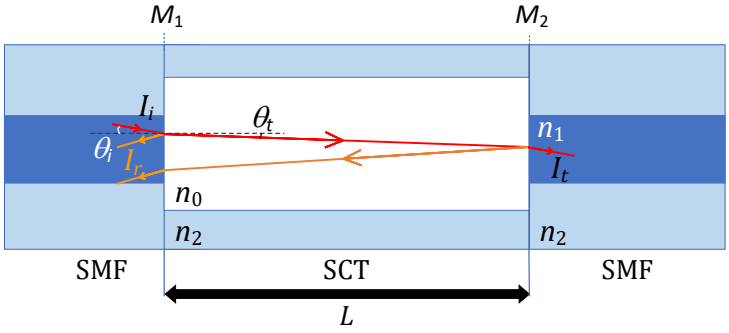

Figure 3.2: Schematic diagram of multiple reflections that constitute an FPI.

This type of FPI has low finesse, a dimensionless quantity that describes the cavity selectivity, due to the low reflectivity of its mirrors. This parameter is given by $R = \left(\frac{n_1 - n_0}{n_1 + n_0}\right)^2$ which, considering the previously defined RIs, results in a reflectivity of ~3.36%. The cavity's finesse is given by $F = 4R/(1-R)^2$, which, for an FPI based on an SCT, is 0.174 [6]. The interferometer can, thereby, be approximated to a two-wave mechanism, owing to successive wave reflections propagating with an intensity so low that it does not contribute to the spectrum.

The optical path difference of adjacent beams is

$$\Lambda = 2n_0 L \cos\theta_t, \tag{3.1}$$

where n_0 is the RI of the air cavity, L is the cavity length, and θ_t is the propagation phase variation of the cavity. For a near orthogonal incidence ($\cos\theta_t = 1$), the phase difference is given by

$$\delta = k\Lambda = \frac{4\pi n_0 L}{\lambda}, \tag{3.2}$$

where the wavenumber, k, is equal to $2\pi/\lambda$, being λ the wavelength of the light signal in free space. The peak wavelength of the FPI is, thus, expressed as [48]

$$\lambda_m^{FPI} = \frac{2L}{m} n_0, \tag{3.3}$$

with *m* corresponding to the resonance order. According to two-beam interference theory, the wavelength spacing between two adjacent peaks is defined as free spectral range (FSR),

$$FSR = \lambda_m - \lambda_{m+1}. \tag{3.4}$$

Using (3.3) and (3.4), the FSR of this interference mechanism is given by

$$FSR_{FPI} = \frac{\lambda_{m+1}\lambda_m}{2Ln_0}. \tag{3.5}$$

The FP interferometry for this configuration is sensitive to the surrounding environment through variation of the capillary length and the hollow core RI, hence why this optical mechanism can be used for sensing purposes.

3.2.2 Antiresonant guidance

The ARROW model involves a structure where the optical fiber is constituted by a low RI layer surrounded by a high RI layer. The latter acts as an FP resonator formed along the radial direction [61].

For the configuration under study shown in Figure 3.3a, the light propagates in the air core and, when encountering the air-silica interface, it can either reflect, remaining in the core, or refract to the silica cladding. The silica cladding will act as an FP resonator, defined by the M_3 and M_4 interfaces. For the AR wavelengths, i.e., wavelengths that do not satisfy the resonant condition, which depends on the geometry of the SCT, destructive interference occurs, and light will be reflected within the resonator and refracted back to the core. Whereas for resonant wavelengths, constructive interference will take place, meaning that the FP resonator is highly transparent for these wavelengths and light does not reflect in the air-silica interface. Instead, it will escape the resonator and leak out from the cladding to the outside of the fiber, resulting in a low transmission intensity part of the spectrum [62]. When the wavelength gradually deviates from the resonant condition, more light is confined in the hollow core of the SCT, reducing the light loss. In Figure 3.3b, two simulated propagating modes in the capillary are represented, using the COMSOL Multiphysics, which depict the antiresonant and resonant wavelengths, respectively.

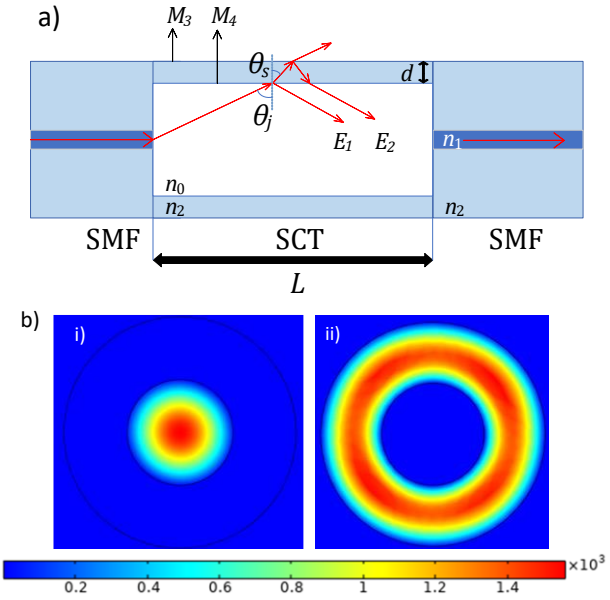

Figure 3.3: (a) Schematic diagram of the interferometry by AR guidance. (b) Simulation in COMSOL Multiphysics of the (i) antiresonant and (ii) resonant mode propagation in the SCT.

The electric field of the light beams, E_1 and E_2, are the incident light reflecting on interface air-silica and silica-air, respectively, with E_2 representing the refracted light that was generated by the first incident light. These two light beams will interfere in the air core with the initial condition that the incident angle is grazing ($\theta_j \approx 90°$). When the phase matching condition of the light beam E_2 is met, it will leak out of the cladding.

The optical path difference of the E_1 and E_2 beams is given by

$$\Lambda = 2n_2 d \cos\theta_s. \tag{3.6}$$

With Snell's law, $n_0 \sin\theta_j = n_2 \sin\theta_s$, and with the fundamental law of trigonometry, one can derive that

$$\cos\theta_s = \sqrt{1 - \frac{n_0^2}{n_2^2}\sin^2\theta_j}. \tag{3.7}$$

Substituting in (3.6), it is obtained that

$$\delta = k\Lambda = \frac{4\pi d}{\lambda}\sqrt{n_2^2 - n_0^2\sin^2\theta_j}. \tag{3.8}$$

If δ is a positive multiple of 2π, and considering a grazing angle ($\theta_j \approx 90°$)[63] then, according to the phase matching condition, the resonant wavelength, λ_m^{AR}, can be given as follows

$$\lambda_m^{AR} = \frac{2d}{m}\sqrt{n_2^2 - n_0^2}, \tag{3.9}$$

where d is the thickness of the FP resonator, in this case, the silica cladding, m is the resonance order and n_2 and n_0 are the RIs of the cladding and air core, respectively.

As to the FSR of the antiresonant guidance phenomenon, it is expressed as

$$FSR_{AR} = \frac{\lambda_{m+1}\lambda_m}{2d\sqrt{n_2^2 - n_0^2}}. \tag{3.10}$$

The length of the SCT is also of great importance in this configuration, as it will determine the generation of this mechanism. When L is sufficiently short, the phenomenon described in the previous section will be dominant in a reflection scheme, resultant from the FP cavity delimited by the interfaces created in the two fusion splices. An increasing SCT length will cause the FP interference to gradually weaken due to space loss. Additionally, in transmission, the FPI exists due to the reflections in the cavity interfering in the lead-out SMF, however, visibility is considerably low [58].

When L is above the critical length (L_c), the AR mechanism begins to take place, both in transmission and in a reflection scheme. Should L increase even further, the AR effect will become dominant. The critical length at which the dominance transition of these two mechanisms occurs is given by the axial transmission length of the E_2 light beam, which is expressed according to the ray optic model

$$L_c = l_1 + 2l_2. \tag{3.11}$$

The model given by equation (3.11) is represented in Figure 3.4

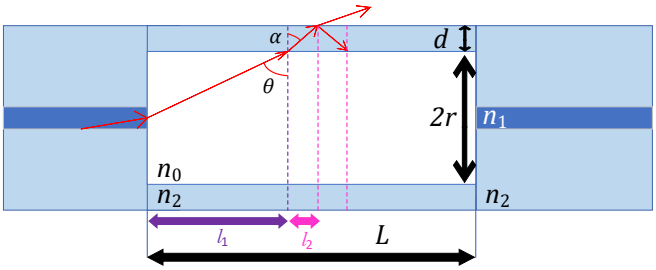

Figure 3.4: Schematic diagram of the critical length based on the ray optic model.

The numerical aperture of an optical fiber can be given by

$$n_0 \sin(90 - \theta) = \sqrt{n_1^2 - n_2^2} \leftrightarrow \cos\theta = \frac{\sqrt{n_1^2 - n_2^2}}{n_0}. \tag{3.12}$$

Using (3.12) and basic trigonometry,

$$l_1 = r\,\mathrm{tg}\,\theta = r\frac{\sin\theta}{\cos\theta} = r\sin\theta\frac{n_0}{\sqrt{n_1^2 - n_2^2}}. \tag{3.13}$$

Analogously, and with Snell's law,

$$l_2 = d\,\mathrm{tg}\,\alpha = d\frac{\sin\alpha}{\cos\alpha} = d\frac{n_0\sin\theta}{n_2\cos\alpha}. \tag{3.14}$$

It is, then, obtained that

$$L_c = n_0\sin\theta\left(\frac{r}{\sqrt{n_1^2 - n_2^2}} + \frac{2d}{n_2\cos\alpha}\right). \tag{3.15}$$

With the fundamental law of trigonometry, Snell's law and some mathematical manipulation, one obtains the final expression of the critical length, which is given by

$$L_c = \sqrt{n_0^2 + n_2^2 - n_1^2}\left(\frac{r}{\sqrt{n_1^2 - n_2^2}} + \frac{2d}{\sqrt{n_1^2 - n_0^2}}\right). \tag{3.16}$$

With that, a capillary length longer than L_c is conducive to the enhancement of the AR effect. Elsewise, only the FPI effect will be excited by the sandwich structure. In the context of this work, the fabricated sensors based on the SCT as a sensing head all possess length greater than L_c.

3.2.3 Mach-Zehnder interferometer

In the sandwich configuration, when the mode field diameter (MFD) of the SMF is within the magnitude order of the size of the SCT air core, the energy in the hollow core and cladding can mutually interfere [58]. Provided that this criterium is met, as light travels through the lead-in SMF into the SCT, it can continue to travel through the hollow core or couple into the cladding, exciting cladding modes that will couple back into the lead-out SMF, which is represented in Figure 3.5.

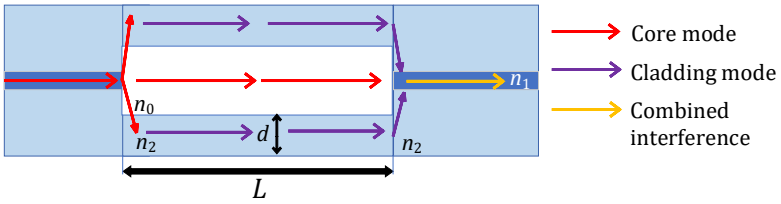

Figure 3.5: Schematic diagram of the cladding and core modes that constitute an MZI in the SCT.

The difference in effective RI of the cladding and the core means that the optical path lengths are different, therefore creating an MZI. According to [58], this interferometer is enhanced when the inner diameter of the SCT is around 10-15 μm. Note that the SMF core diameter is, typically, ~8.2 μm and the MFD is (10.5 ± 0.5) μm at 1550 nm [64]. The optical path difference between the cladding and core modes is given by

$$\Lambda = L \times (n_2 - n_0). \tag{3.17}$$

The phase difference is given by

$$\delta = \frac{2\pi \Delta n L}{\lambda}, \tag{3.18}$$

where Δ*n* is the difference between the effective RIs. In this case, destructive interference will occur when the phase difference becomes an odd multiple of π, thus the dip wavelength can be expressed as

$$\lambda_m^{MZI} = \frac{2\Delta n L}{2m+1}. \tag{3.19}$$

While the FSR of this interferometer is given by

$$FSR_{MZI} = \frac{\lambda_{m+1}\lambda_m}{\Delta n L}. \tag{3.20}$$

The Table 3.1 congregates the equations that define the peak wavelengths and FSR of different interferometers. It is interesting to observe a dependance of the peak wavelength on the length of the sensor for the FPI and MZI interferometers, while the AR does not depend on this quantity. Additionally, the FPI peak wavelength is influenced only by the core RI while the AR and MZI also show dependance on the cladding RI. Insofar as the FPI is concerned, solely variations inside of the cavity will induce wavelength shifts, whereas the AR and MZI phenomena will exhibit wavelength shifts introduced by variations in the cladding. This particularity can lead to different sensitivities of the interferometers concerning the same measurand, which is crucial to the development of hybrid sensors.

Table 3.1: Peak wavelength and FSR of different interference mechanisms in the sandwich structure.

Mechanism	λ_m	FSR
FPI	$\frac{2L}{m}n_0$	$\frac{\lambda_{m+1}\lambda_m}{2Ln_0}$
AR	$\frac{2d}{m}\sqrt{n_2^2 - n_0^2}$	$\frac{\lambda_{m+1}\lambda_m}{2d\sqrt{n_2^2 - n_0^2}}$
MZI	$\frac{2\Delta nL}{2m+1}$	$\frac{\lambda_{m+1}\lambda_m}{\Delta nL}$

In the following Chapters, three different fiber sensors will be described and characterized to several parameters. The first studied sensor follows an SMF-SCT-SMF/SCT configuration with additional access channels instilled on the fiber, enhancing an FPI and AR. Pressure and temperature measurements were achieved for this sensor in a reflection scheme. The second fiber sensor that is explored has, likewise, the sandwich configuration which is bent in a balloon-like shape enhancing an MZI and AR. For the balloon-like sensors, a characterization to displacement and temperature was realized in a transmission scheme. Finally, the third sensor configuration is an SMF-HSCF-SCT which excited up to three FP cavities. The sensor was able to achieve a simultaneous multiparameter detection of pressure, temperature, and curvature.

4. Hybrid sensor based on FPI + AR

4.1 Sensor design

The sensors developed to perform simultaneous measurement of pressure and temperature were based on an SCT made of pure silica, fabricated at Leibniz-IPHT in Jena, Germany, with the stack and draw method. The SCT used in this work has an inner diameter of (57 ± 2) µm and an outer diameter of ~125 µm (Figure 4.1a). The external coating is made of acrylate and its thickness is 60 µm. By solving equation (3.16) with the physical dimensions of this SCT, the critical length obtained is ~300 µm.

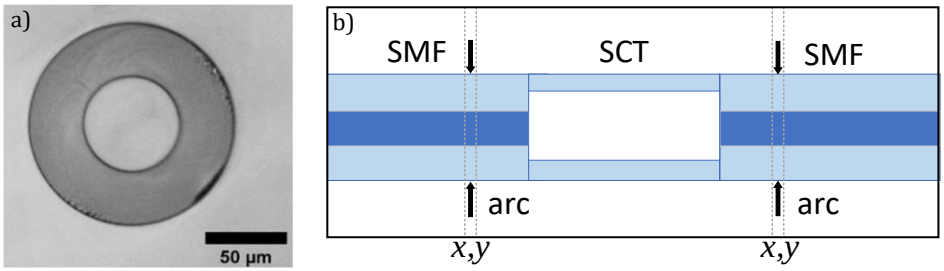

Figure 4.1: (a) Cross-section view of the silica tube on a microscope. (b) Splicing process between an SMF and an SCT.

In order to obtain the desired configuration, it is necessary to perform the splices with particular care. The splice between one end of a fiber with the end of another was made with the splicing machine Fujikura FMS-40S in the manual mode with a power of 15 bits (arbitrary unit) and an arc time of 500 ms. Comparatively, the automatic mode has a power of 25 bits and an arc time of 2000 ms, and it performs the fiber alignment through their cores. The splicing power in this mode is too high and it would damage the SCT, undermining the quality of the splices. Additionally, since the SCT has a hollow core, the alignment would not have been attainable, therefore it is necessary to opt with the manual mode. The splicing parameters were established through trial-and-error experiments.

Once the manual mode is selected, two SMFs are placed in the splicing machine and an automatic alignment is performed. Then, one of the fibers is replaced with the SCT and a manual alignment is employed by approximating the fibers as much as possible from one another with the left and right motors and along the *x* and *y* axes. Before applying a final arc, it is necessary to move the SCT away from the electrodes so as not to collapse its core. This offset allows the arc discharge to primarily occur in the SMF, as depicted in Figure 4.1b.

To obtain the desired capillary length, the SCT segment is then cleaved with a fiber cleaver with the help of a digital microscope for higher accuracy – around ± 20 µm. Finally, the splicing process is repeated for the free end of the SCT with another SMF, or to a different SCT, a method that will be discussed in the following section when an access channel is required.

The following studied sensor is composed by the sandwich configuration wherein access channels were instilled on the fiber. Pressure and temperature measurements were achieved for this sensor in a reflection scheme.

4.2 Creating access channels

In an effort to grant the sensor responsiveness to pressure, it is necessary to create an access channel that allows gas entrance through the channel into the structure. This was developed in two distinctive manners, the first being the creation of a bubble on the capillary. This bubble is an air cavity that is achieved in the fusion splicer by performing several successive arcs on the capillary whilst under pressure. For this purpose, the parameters used in the manual mode were a power of 20 bits with a first arc of 1300 ms and rearcs of 700 ms, under a pressure of approximately 270 mbar.

Firstly, two SMFs are placed in the fusion splicer, and the alignment is done, followed by replacing them with a long segment of the SCT. One end is glued with UV curable resin to a 0.3 mm PTFE tube that is connected to a microfluidic system from Bartels^{TM} controlled by an Arduino with an electronic pressure sensor. The other end is glued to a PTFE tube connected to a syringe, where the compression of its piston increases the pressure in the capillary. Once the desired pressure is achieved, the electric arc discharges can be employed. The first arc locally heats up the fiber, causing it to expand in the electrodes area. As the expansion persists, the pressure in the capillary causes the fiber to tear up and a bubble appears, creating a micro gas inlet into the capillary. With each subsequent re-arc the bubble attains a rounder, more spherical shape and the fiber stretches and becomes straighter, without strain. This process is repeated until the desired shape is obtained. The experimental is illustrated in Figure 4.2 together with a diagram of the bubble formation stages.

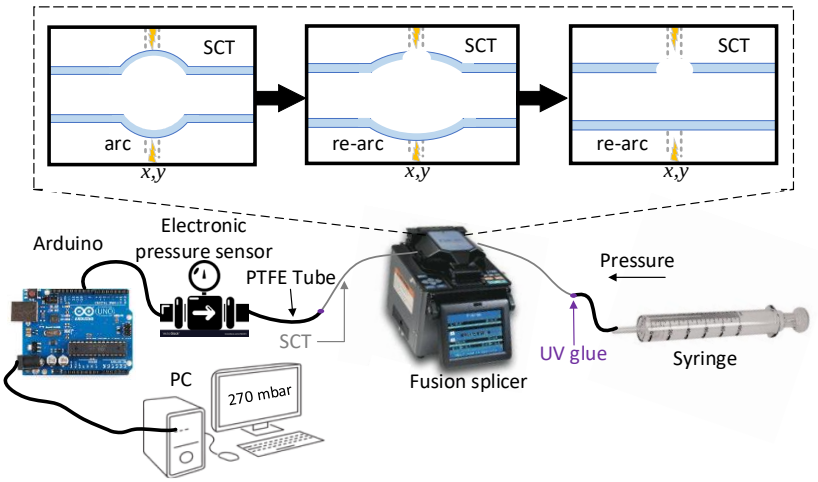

Figure 4.2: Schematic diagram of the bubble formation stages and setup by performing several successive arcs on the capillary whilst under pressure of ~270 mbar.

Another method of developing an access channel is by splicing the capillary with another capillary of different inner diameter instead of a second SMF. Hence, the access channel is located on the free end of the second capillary in its hollow core. For clarity, in this section the sensing head shall be denominated as thick core SCT, while the second capillary will be denoted as thin core SCT. The thin core SCT used for this purpose has a diameter of ~20 µm. This small inner diameter was chosen so that it does not interfere with the mirror defined by the thin core SCT- thick core SCT interface, while being large enough not to collapse during splicing. By splicing a thick core SCT that contains a bubble with a thin core SCT, a two-access channel fiber sensor is obtained, as illustrated in Figure 4.3.

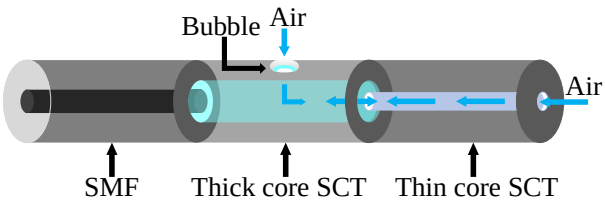

Figure 4.3: Schematic diagram of a two access channel fiber sensor.

Figure 4.4 shows the microscopic view of several small sensors based on the sandwich configuration. Figure 4.4a reveals a closed capillary with a length of 609 µm. In Figure 4.4b, the 600 µm long capillary contains a bubble that acts as an access channel whereas in Figure 4.4c the access channel was achieved by splicing the 547 µm long capillary with an SMF and another SCT. Finally, in Figure 4.4d, a two access channel 800 µm long sensor is depicted that combines the bubble and thin capillary in the sensor configuration. Contrary to what the Figure 4.4b suggests, the channel is not closed by the SCT external wall. The fiber position in relation to the microscope does not allow a clear observation of the access channel. This bubble has an approximate diameter of 40 to 50 µm.

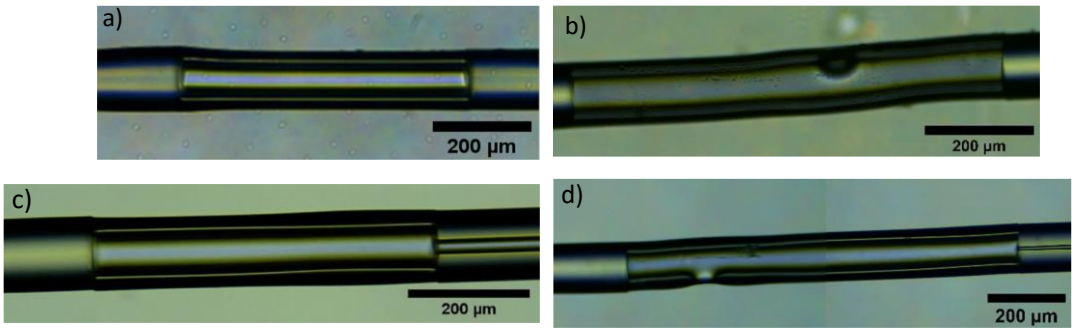

Figure 4.4: Microscopic view of: (a) SMF-capillary-SMF; (b) Access channel: bubble created on the capillary; (c) SMF-Thick core SCT-Thin core SCT; (d) Two access channel fiber sensor: bubble and thin core SCT.

4.3 Experimental Setup & Spectral Characterization

There are three components necessary to achieve a fiber sensor functionality: a light source (transmitter), the fiber sensor and a signal acquiring system (receptor). The sensor characterization can be done in a transmission or reflection configuration. The broadband light source used emits on the C+L band, having a central wavelength of 1570 nm and a broad bandwidth of 80 nm. As for the receptor, an optical spectrum analyzer (OSA, Anritsu, model MS9740A)) was used, with a maximum resolution of 30 pm. This resolution can be changed, as well as other parameters like sample size, frequency, and wavelength span. For broad spectra acquisition, a resolution of 0.05 nm and a sample size of 2001 points was used. In a reflection analysis, one end of the sensor is connected to an optical circulator which, in turn, connects to the source and OSA (Figure 4.5). Before the spectrum was acquired, a normalization to the source was performed.

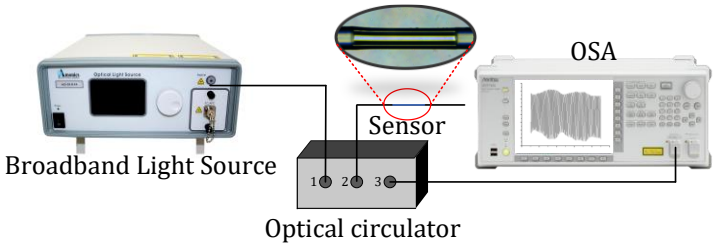

Figure 4.5: Experimental setup for spectral analysis in a reflection configuration.

The reflection spectra of the sensors with 0, 1, and 2 access channels were obtained, for a long sensing length of ~2 mm, which is much greater than the critical length, and for short sensors with lengths between 600 µm and 1000 µm, as depicted in Figure 4.6.

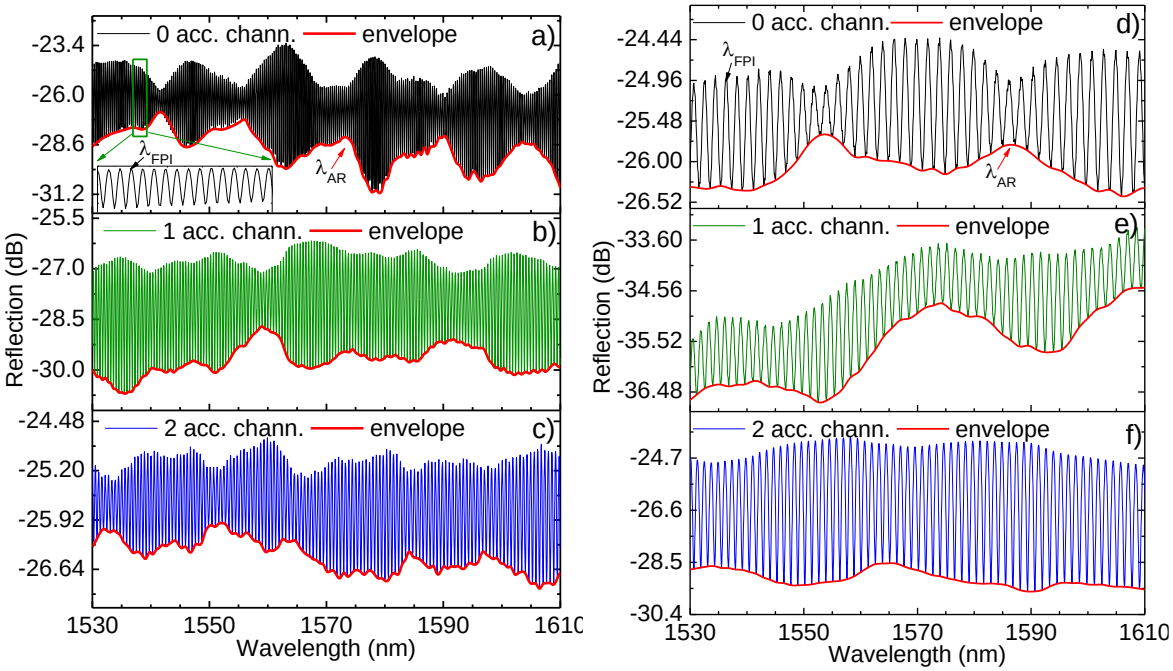

Figure 4.6: Reflection spectrum of the long sensors with (a) 0, (b) 1, and (c) 2 access channels and the short sensors with (d) 0, (e) 1, and (f) 2 access channels. Inset in (a): Zoom-in in the 1530-1535 nm region.

Two signals with different oscillation frequencies can be seen simultaneously in the reflection spectrum. The high frequency oscillation corresponds to the FPI which is modulated by a low frequency oscillation, the AR. The latter is extracted from the spectrum through usage of an envelope analysis tool, as depicted by the red lower line that circumvents the spectrum. It can be seen a decrease in visibility as additional access channels were instilled on the fiber sensors. Additionally, comparing the acquired spectra of shorter sensors in Figure 4.6(d-f) with their longer counterparts in Figure 4.6(a-c), an increase of the FSR for the FPI spectrum can be seen, which is expected to depend on *L* according to (3.5). It can, also, be observed a decrease in the envelope amplitude as well as less defined AR peaks, which is due to the sensors possessing a length closer to critical. Though in literature the visibility of the AR appears not to have a clear dependance on length, the experimental results are still comparable with the ones already reported [48].

When obtaining the reflection spectra of sensors with access channels, it is unsurprising that a phenomenon involving propagation in the cladding, which is the case of the AR, reveals less definition in its low frequency oscillations, not only in regards to the shape of the dips but also in terms of amplitude. Due to the process of instilling a bubble on the capillary which entails cladding deformation and the introduction of an irregular element in the cladding, the resulting envelope for these sensors' spectra is less shapely than that of a closed sensor. Concerning the shorter sensors, the antiresonance conditions are put into question, as they are closer to the critical length. Ascertain that, as seen in equation (3.16), this quantity depends on the cladding thickness, which could be locally deformed for a sensor with a bubble. In order to evaluate this hypothesis, a transmission measurement would be required. Howbeit, the sensing configuration does not permit such analysis scheme for sensors with a thin core SCT.

Finally, when searching for the optimal sensing length, a compromise must be made between the interferometric spectral response. When the SCT is considerably longer than L_c, the AR spectrum is more defined and easier to analyze. However, the sensor possesses higher losses and a smaller FSR of the FPI spectrum. Thus, the monitorable capillary length is limited by the resolution of the OSA towards the FPI. On the other hand, SCTs with length that is closer to (but still greater than) L_c showcase a reflection spectrum with a nicely spaced FPI, with the drawback that the AR conditions are worsened, thus, its spectrum is less defined, making it harder to monitor.

Apropos of the different techniques towards the fabrication of inlet/outlet that allow fluids to enter the fiber sensors, previous studies have often used femtosecond laser micromachining [47,48,65] which enhances the complexity of the sensor fabrication as well the associated cost, limiting their mass production and practical applications. Other techniques include using C-shaped fibers which were shown to allow the entrance of water, and butt-coupling, which displays a gap between two fibers so that fluids can interact with the hollow core. According to [66], this method requires precise splicing, meticulous alignment and renders the system less compact, robust, and reliable when compared with the aforementioned techniques. A different tool for this purpose is the focused ion beam milling of cavities which has high beam current, accuracy in the nanometer range and controllable spot size. However, this method can unintentionally ion dope the substrate, redeposition material and has considerable associated cost [67,68].

4.4 Characterization of the sensors

For each sensor, with and without access channels, pressure and temperature measurements were performed. By selecting a certain peak of the interferometers and following it throughout the measurand variation, a wavelength shift will be obtained. The slope of the linear fitting of the experimental points given by the wavelength shift against the parameter variation gives the sensitivity of the sensor.

4.4.1 Characterization to Pressure

The sensors were characterized to pressure in a closed chamber that was fabricated in-house. The experimental setup given in Figure 4.7 includes a chamber with two valves and two connectors. One valve is attached to a compressed gas system that lets the air in, increasing pressure, while the other valve allows the air to escape the chamber, decreasing its pressure. The connector allows the coupling between the sensor inside the chamber and an outside cable, which is then connected to an interrogation system. Thus, it is possible to use a configuration in reflection and transmission. The chamber is connected to an electronic pressure and temperature reading system through the software KOLIBRI desktop.

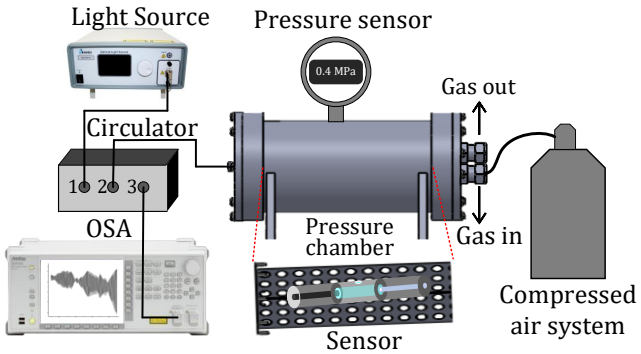

Figure 4.7. Schematic diagram of the pressure experimental setup.

Pressure measurements between 0 and 0.4 MPa were made with steps of 0.05 MPa, wherein the resolution of the electronic pressure sensor is of 0.0001 MPa. For such, after the sensor was placed in the chamber, the latter was sealed and filled with air until the pressure hit 0.4 MPa, then the second valve was opened until the pressure lowered by 0.05 MPa, acquiring and saving the spectrum at every descending pressure step. This process reveals higher linearity in pressure variation than with increasing pressure steps. Additionally, valve manipulation towards gas release is far less cumbersome than handling the compressed air system and its attached valve.

In Figure 4.8a, where sensors with ~2 mm length were characterized, it is visible that the closed sensor (FPI_0chann. and AR_0chann.) is insensitive to pressure for both FPI and AR. For open sensors, the FPI showcases a shift towards longer wavelengths (red shift) while the AR component pertains a shift towards shorter wavelengths (blue shift). Furthermore, smaller sensors were characterized to pressure in an identical manner. These sensors possess a capillary length ranging from 600 to 1000 µm. Coherently, a closed sensor and two open sensors, with one and two access channels, were characterized.

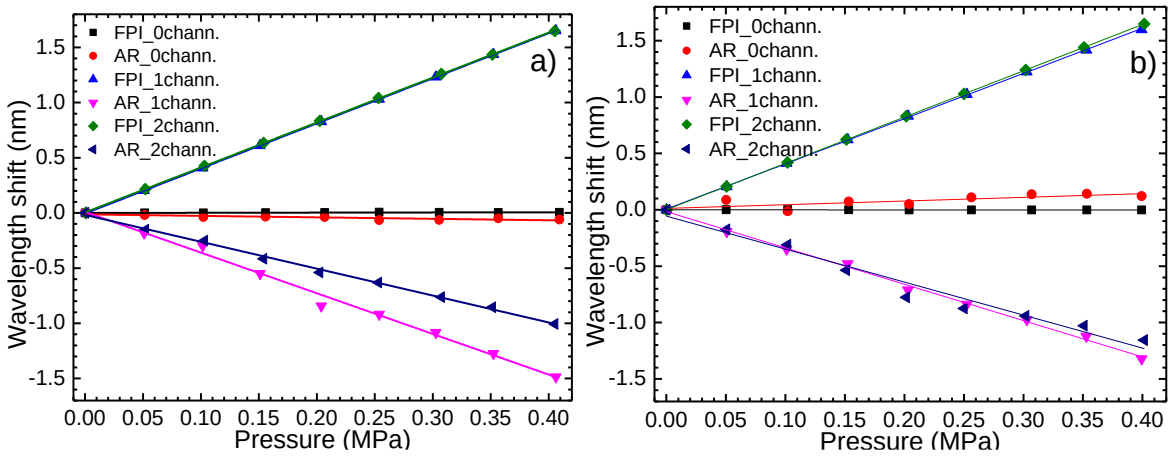

Figure 4.8: Pressure characterization for 3 sensors with 0, 1, and 2 channels with length (a) L ~ 2 mm and (b) L ~700 µm.

For open sensors the sensitivities to FPI were the same while for AR the sensitivity for 1 channel was greater (in module) than for 2 channels as depicted in Table 4.1. Generally, high linearity was observed. A similar and comparable behavior is observed in Figure 4.8b with the pressure characterization of smaller sensors with the difference that the sensitivities of the sensors with 1 and 2 access channels are quite similar for both interferometers, including for AR which was not the case for the longer sensors. In fact, resolution limitations can be inferred from the lower linearity evidenced in the AR response of shorter length sensors. Nevertheless, the sensitivity of the AR of 1 access channel is, still, greater than the sensitivity of AR for 2 access channels. The obtained sensitivities are summarized in Table 4.1.

Table 4.1: Sensitivities of the sensors to pressure.

Sensor	Length (µm)	κ_{FPI} (nm/MPa)	R^2_{FPI}	κ_{AR} (nm/MPa)	R^2_{AR}
0 channels	2000	0.015 ± 0.004	0.6067	-0.13 ± 0.03	0.7103
	609	-0.006 ± 0.001	0.7875	0.33 ± 0.09	0.5846
1 channel	2400	4.085 ± 0.004	0.9999	-3.7 ± 0.1	0.9915
	792	4.01 ± 0.02	0.9998	-3.22 ± 0.07	0.9966
2 channels	2100	4.07 ± 0.01	0.9999	-2.44 ± 0.05	0.9969
	973	4.105 ± 0.003	0.9999	-2.9 ± 0.2	0.9650

Albeit a lower linearity of the shorter sensors was attained than that for 2-mm-long sensors, the results obtained remain comparable. Furthermore, a comparison study was carried out for the pressure response of the 1 access channel 2-mm-long sensors with a bubble vs a thin core SCT as seen in Table 4.2. It was found that having either optical structure attains the same results with similar linearity, thus validating both methods for fabricating access channels.

Table 4.2: Sensitivities of the 1 access channel sensors to pressure.

1 acc. chann. sensor	κ_{FPI} (nm/MPa)	R^2_{FPI}	κ_{AR} (nm/MPa)	R^2_{AR}
Bubble	4.085 ± 0.004	0.9999	-3.7 ± 0.1	0.9915
Thin core SCT	4.071 ± 0.005	0.9999	-3.76 ± 0.08	0.9961

The reason for the different pressure sensitivities can be understood as follows. Regarding the FPI, the pressure sensitivity primarily derives from the RI variation of the core since the change in the sensing length is neglectable. Thus, one can derive from equations (3.3) the FPI pressure sensitivity

$$\frac{\partial \lambda_{FPI}}{\partial P} = \frac{2L}{m}\frac{\partial n_0}{\partial P} + \frac{2n_0}{m}\frac{\partial L}{\partial P} = \left(\frac{1}{n_0}\frac{\partial n_0}{\partial P} + \frac{1}{L}\frac{\partial L}{\partial P}\right)\lambda_{FPI} \tag{4.1}$$

Where inline sensors are concerned, the length variation is low, therefore the first term of equation (4.1) is dominant. The pressure sensitivity of the AR component of this sensor is an accumulation of three factor contributions: (i) RI variation in the hollow core S_{air}, (ii) structural deformation of the silica cladding $S_{structure}$, and (iii) RI change of silica cladding as a result of the deformation in (ii) due to the strain-optic effect, S_{silica}. The AR pressure sensitivity, derived from (3.9), is given by

$$\begin{aligned}\frac{\partial \lambda_{AR}}{\partial P} &= S_{air} + S_{structure} + S_{silica} \\ &= -\frac{2dn_0}{m\sqrt{n_2^2 - n_0^2}}\frac{\partial n_0}{\partial P} + \frac{2\sqrt{n_2^2 - n_0^2}}{m}\frac{\partial d}{\partial P} + \frac{2dn_2}{m\sqrt{n_2^2 - n_0^2}}\frac{\partial n_2}{\partial P} \\ &= \left(-\frac{n_0}{n_2^2 - n_0^2}\frac{\partial n_0}{\partial P} + \frac{1}{d}\frac{\partial d}{\partial P} + \frac{n_2}{n_2^2 - n_0^2}\frac{\partial n_2}{\partial P}\right)\lambda_{AR}\end{aligned} \tag{4.2}$$

The refractive index of the air depends on pressure and temperature according to [47]:

$$n_0 = 1 + \frac{2.8793 \times 10^{-9} \times P}{1 + 0.003661 \times T}, \tag{4.3}$$

where *P* and *T* are the pressure and temperature, respectively. Therefore, an increase in pressure results in an increase of n_0. This variation is the dominant contribution for the attained sensitivities. According to the equations (3.3) and (3.9), it is theoretically predicted that the FPI will showcase a positive wavelength shift while the AR will suffer a shift towards shorter wavelengths. Considering $\lambda_{FPI} \approx 1550\ nm$ and a temperature of 25 ºC, the first term of equation (4.1) results in a sensitivity of the FPI of 4.089 nm/MPa, which is close to the experimental sensitivity, corroborating the fact that it is the main contribution for pressure sensitivity. Similarly, the value of S_{air}, considering $\lambda_{AR} \approx 1555\ nm$, was obtained as -3.78 nm/MPa, revealing, once again, the dominance of this term.

When comparing the AR sensitivity of a sensor with one and two access channels, the decrease observed for the two access channel sensor may be due to the pressure flow established between the channels, inducing greater structural deformation of the silica cladding.

4.4.2 Characterization to Temperature

For temperature characterization, the experimental setup involved a Peltier cooler placed on a dissipation block, connected to a temperature controller. The Peltier Effect is based on the production of a temperature difference in a junction of two semiconductors of distinct materials when submitted to a potential difference in a closed circuit [69]. The fiber was placed on the dissipation block with the sensing element leaning on the Peltier, as shown in Figure 4.9.

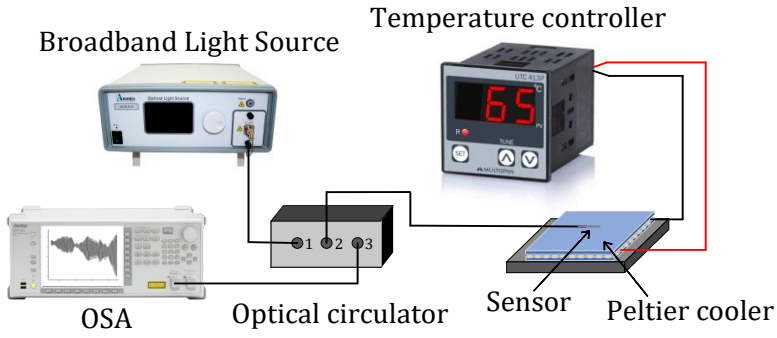

Figure 4.9: Schematic diagram of the temperature setup using a Peltier cooler.

The temperature controller (Thorlabs, TED350) has a resolution of 0.1 °C. To characterize the sensors to temperature, increments of 5 °C within the range of 20 – 80 °C were performed. The spectra were obtained on each temperature step, for increasing and decreasing temperatures in this range.

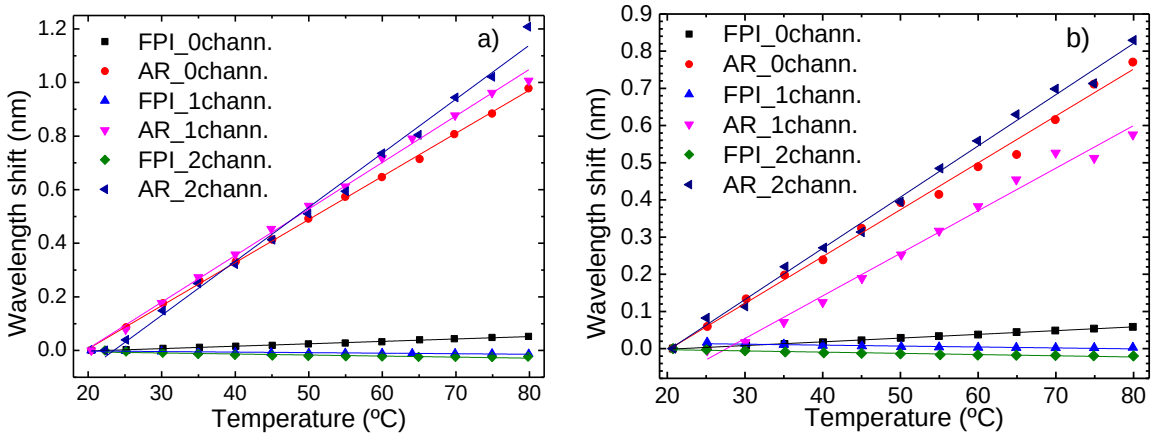

Figure 4.10: Temperature characterization for 3 sensors with 0, 1 and 2 channels with length (a) L ~ 2 mm and (b) L ~ 700 µm.

It is visible in Figure 4.10 that the AR pertains a red shift with much greater sensitivity than that of the FPI. The latter was positive on the closed sensors and negative on the open sensors, however it is practically insensitive for both sensors. The attained sensitivities are shown in Table 4.3.

Table 4.3: Sensitivities of the sensors to temperature.

Sensor	Length (µm)	κ_{FPI} (pm/°C)	R^2_{FPI}	κ_{AR} (pm/°C)	R^2_{AR}
0 channels	2000	0.90 ± 0.02	0.9956	16.1 ± 0.1	0.9993
	609	1.00 ± 0.01	0.9979	12.6 ± 0.3	0.99373
1 channel	2400	-0.20 ± 0.02	0.9108	17.4 ± 0.3	0.9974
	792	-0.25 ± 0.03	0.82791	11.5 ± 0.4	0.98764
2 channels	2100	-0.39 ± 0.05	0.80701	20.2 ± 0.5	0.99362
	973	-0.33 ± 0.03	0.91762	13.8 ± 0.3	0.99489

Since the sensitivity in FPI is quite trifling and the temperature range is short, the resolution is insufficient to correctly determine these coefficients. Notwithstanding, a good linearity is evidenced in the results for both interferometers. Similarly, a low FPI sensitivity is evidenced for the short sensors with a red shift for the AR monitoring, whose sensitivity was lower than that for longer sensors.

As a response to an applied temperature rise, the material suffers an expansion – given by the thermal expansion coefficient (TEC) – and a RI variation – given by the thermo-optic coefficient (TOC). For silica these coefficients are ~5.56 × 10^{-7} /°C and ~8.6 × 10^{-6} /°C, respectively [15]. On the other hand, the FPI cavity is made of air, whose RI practically does not vary with temperature. Therefore, the FPI sensitivity to temperature is expected to be low. Since on equation (3.9) for AR there is a dependence on d and n_2, not only is the sensitivity positive, but it is also much greater than the FPI sensitivity.

$$\frac{\partial \lambda_{FPI}}{\partial T} = \frac{2L}{m}\frac{\partial n_0}{\partial T} + \frac{2n_0}{m}\frac{\partial L}{\partial T} = \left(\frac{1}{n_0}\frac{\partial n_0}{\partial T} + \frac{1}{L}\frac{\partial L}{\partial T}\right)\lambda_{FPI}, \tag{4.13}$$

$$\begin{aligned}\frac{\partial \lambda_{AR}}{\partial T} &= \frac{2\sqrt{n_2^2 - n_0^2}}{m}\frac{\partial d}{\partial T} + \frac{2dn_2}{m\sqrt{n_2^2 - n_0^2}}\frac{\partial n_2}{\partial T} = \left(\frac{1}{d}\frac{\partial d}{\partial T} + \frac{n_2^2}{n_2^2 - n_0^2}\frac{1}{n_2}\frac{\partial n_2}{\partial T}\right)\lambda_{AR} \\ &= \left(\alpha + \frac{n_2^2}{n_2^2 - n_0^2}\beta\right)\lambda_{AR},\end{aligned} \tag{4.14}$$

where α and β are the silica's TEC and TOC, respectively. It is, now, possible to predict the temperature sensitivity for both components. It was considered $\lambda_{FPI} \approx 1560\, nm$ and $\lambda_{AR} \approx 1555\, nm$. Values of ~0.87 pm/°C and ~26.5 pm/°C were respectively obtained for FPI and AR, which are quite proximate to the experimental ones. The variations evidenced may be due to approximations previously considered. Notice that the thermo-optic effect is dominant in the AR while the thermal expansion is the dominant effect in the FPI. Furthermore, the attained results are comparable with those found in literature [70].

The presence of an access channel does not, theoretically, change the sensitivity to temperature of the capillary-based sensor. While the RI of air is subject to change due to pressure and temperature change, as seen in equation (4.3), the system was kept isolated during temperature variation, so that pressure would remain constant throughout the experiment. There are, however, limitations that originate from the experimental setup since the sensors with a thin core SCT reveal an access channel that is not under the influence of the Peltier, thus allowing the entrance of colder air in the fiber, influencing the temperature detection results. This problem would possibly be overcome by using a setup involving a climatic chamber where the entirety of the fiber sensor is under the same temperature.

4.4.3 Hybrid measurements

For fiber sensors in which two or more interferometers occur, ofttimes a matrix method is used for simultaneous measurements, that assumes the verification of two conditions. One is that the dependance of the interferometers is linear with the measured parameters. The other condition is that each sensing mechanisms has different sensitivities to each parameter [17].

When a pressure (ΔP) and temperature variation (ΔT) occur in the surrounding environment, the reflection spectrum of the sensor will shift accordingly. Should this shift pertain a linear variation, the wavelength shifts of the FPI and AR can be expressed as

$$\Delta\lambda_{FPI} = \kappa_{FPI}^{\mathrm{P}}\Delta P + \kappa_{FPI}^{\mathrm{T}}\Delta T, \tag{4.15}$$

$$\Delta\lambda_{AR} = \kappa_{AR}^{\mathrm{P}}\Delta P + \kappa_{AR}^{\mathrm{T}}\Delta T, \tag{4.16}$$

where κ_i^j is the sensitivity of the studied interferometer, i, FPI and AR, of the corresponding measurand, j, pressure and temperature. Thus, the total wavelength shift of each interferometer is the sum of the shifts for each measurand. Since the sensitivities of the interferometers (FPI and AR) were different for both parameters, a hybrid application of the sensor can be made for simultaneous measurement of pressure and temperature by tracing the wavelength shift of each interferometer and solving the following matrix

$$\begin{bmatrix}\Delta\lambda_{FPI}\\ \Delta\lambda_{AR}\end{bmatrix} = \begin{bmatrix}\kappa_{FPI}^{P} & \kappa_{FPI}^{T}\\ \kappa_{AR}^{P} & \kappa_{AR}^{T}\end{bmatrix}\begin{bmatrix}\Delta P\\ \Delta T\end{bmatrix} \Longrightarrow \begin{bmatrix}\Delta\lambda_{FPI}\\ \Delta\lambda_{AR}\end{bmatrix} = \begin{bmatrix}4.085 & -0.0002\\ -3.7 & 0.0174\end{bmatrix}\begin{bmatrix}\Delta P\\ \Delta T\end{bmatrix}. \tag{4.17}$$

By calculating the inverse matrix, the variation of pressure and temperature is, therefore, given by

$$\begin{bmatrix}\frac{\Delta P}{\Delta T}\end{bmatrix} = \frac{1}{0.07022}\begin{bmatrix}0.0174 & 0.0002\\ 3.7 & 4.085\end{bmatrix}\begin{bmatrix}\Delta\lambda_{FPI}\\ \Delta\lambda_{AR}\end{bmatrix}. \tag{4.18}$$

where $D = \kappa_{FPI}^{P}\kappa_{AR}^{T} - \kappa_{FPI}^{T}\kappa_{AR}^{P} = 0.07022$ is the determinant of the inverse matrix. It is, thus, clear that, in order to implement this method, $D \neq 0$. The resolution measurement of these parameters can be assessed by fixing pressure while varying temperature and keeping temperature fixed while changing pressure. Using equation (4.18), the ideal and experimentally obtained values of pressure and temperature can be compared, whose discrepancy yields the resolution of each parameter, defining the degree of independence towards hybrid measurements.

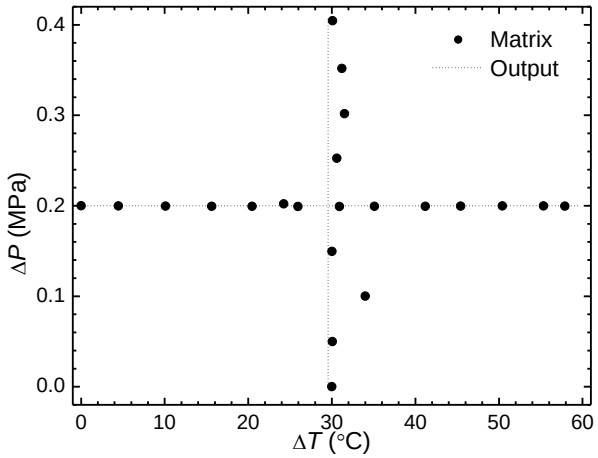

Figure 4.11: Sensor output of simultaneous measurement of pressure and temperature for a 2 mm, 1 access channel SCT-based sensor.

From Figure 4.11 it is evidenced a great perpendicularity between both parameters, highlighting a very linear response in the pressure component, whilst the temperature output reveals a maximum deviation of ~4 °C at 0.1 MPa which arises from the different orders of magnitude of the pressure and temperature sensitivities. The standard deviation of each parameter gives the resolution of simultaneous measurements. The obtained resolutions for this sensor were ± 2.6×10^{-4} MPa and ± 2.6 °C for pressure and temperature, respectively.

5. Balloon-like hybrid fiber sensor based on MZI + AR

5.1 Sensor design and fabrication

The balloon-like fiber sensor is based on an SMF-SCT-SMF configuration with an arch shape wherein the SCT is placed at the top-center position of the balloon and the SMFs are fed through a Tygon® capillary tube that is positioned accordingly.

The fabrication method is similar to that employed in Section 4.1. For this kind of configuration, however, stronger splices were required that could withstand the forced bending. The chosen parameters consisted of a power of 20 arb. un. and an arc time of 1500 ms. The offset was also not performed during these splices in order to further strengthen them, increasing their breaking point as curvature is increased in the balloon. These parameters were chosen in a compromise between stronger splices that can withstand smaller bending diameters, without collapsing the sensor at the junction of the SMF and the SCT.

The capillary length chosen was of the centimeters order. Thereby the antiresonance spectra will be more evident – that is, with better defined dips and with higher visibility - and no FPI will arise, as the measurements will be acquired in a transmission configuration for a long capillary length.

Once the splices were finished, the two ends of the SMFs were joined in a small segment of a Tygon® capillary tube that was moved upwards and adjusted until the fiber had an arch shape, commonly referred to as a balloon, ensuring that the SCT would be at the center of this arch. The length, bending diameter, and radius of the balloon are termed L_b, d_b, and r_b, respectively, as depicted in Figure 5.1a. Once the desired bending diameter was obtained, the fiber was glued on both tips of the Tygon® capillary tube with UV curable resin, whose real picture is depicted in Figure 5.1b.

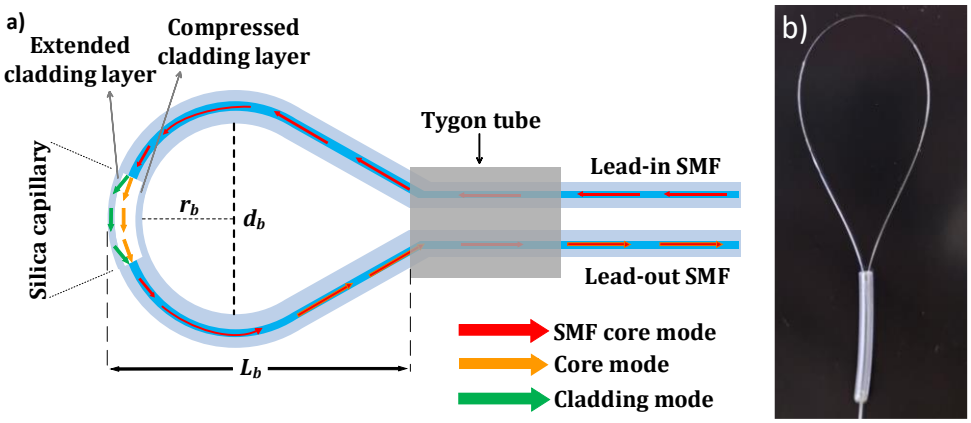

Figure 5.1: (a) Schematic diagram of the balloon-like interferometer. (b) Picture of the fabricated sensor.

As seen in section 3.2.3, in order for an MZI to be created in this configuration for a straight, unbent fiber, the SCT inner diameter is required to be within the order of magnitude of the MFD of the SMF, which is not the case for the one used in this work. However, the bending introduced in the fiber, consequence of the balloon-shape, enabled the enhancement of this interferometer.

When the light propagates through the lead-in SMF to the bending section, upon reaching the SCT instead of normally continuing its free path through its core, the bending of the fiber forces a portion of the light to penetrate into the extended cladding, exciting the cladding modes, later coupling back to the core of the lead-out SMF, which results in the enhancement of an MZI.

5.2 Spectral Characterization

A typical transmission configuration for spectral analysis of the balloons was used where one end of the fiber sensor is connected to the source and the other end to the OSA (Figure 5.2).

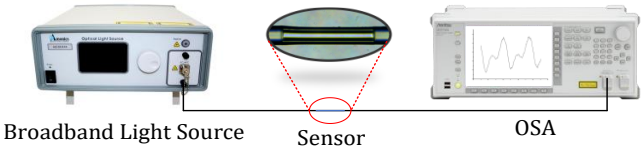

Figure 5.2: Experimental setup for spectral analysis in a transmission configuration.

The transmission spectrum of a (1.2 ± 0.1)-cm-long fiber sensor with no curvature, completely straight, reveals only well-defined periodic AR dips. In a balloon configuration with large length this result persists, however, as the balloon becomes smaller, the curvature on the SCT increases until a point where a low visibility, high frequency oscillation appears in the spectrum, corresponding to the MZI, as seen in Figure 5.3a at 6.3 cm balloon length. A smaller bending diameter results in more light penetrating into the cladding mode, resulting in an increase in the visibility of the MZI dips, as shown in Figure 5.3a for balloon lengths of 5.6 and 4.0 cm. The increase of visibility is desired as it allows for an enhancement in resolution for sensing. However, if the bending diameter continues to decrease, an excess of light will penetrate into the cladding and even leak out of the fiber, resulting in large attenuation [71].

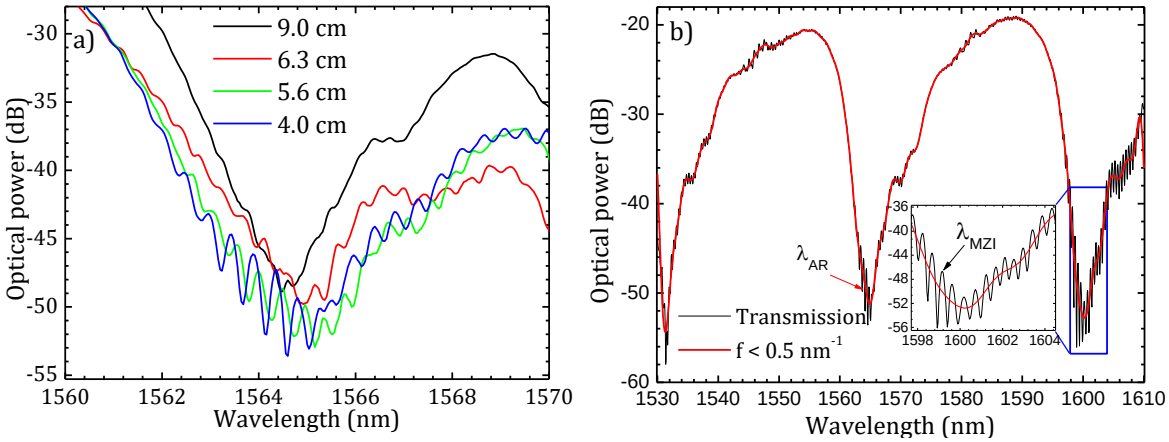

Figure 5.3: a) Transmission spectra for a 1.2 cm sensor with different balloon lengths. (b) Original spectrum and low pass filter of the sensor for a 4 cm balloon length.

For a 4 cm balloon length (bending diameter of 21.9 mm), the MZI is present throughout most of the spectrum. In order to obtain only the AR dips, a 0.5 nm^{-1} low pass filter was applied, as is depicted in Figure 5.3b. The frequency of the filter was chosen based on this sensor's transmission spectrum FFT, as shown in Figure 5.4, where the AR region corresponds to the rectangle in green. The MZI region has a higher frequency and is given by the lilac rectangle. In this sensor configuration, an MZI is present at balloon lengths as big as 8.5 cm which is equivalent to a 45 mm bending diameter. This bending diameter is greater than the values presented by other works, with the highest found to be 14 mm [72].

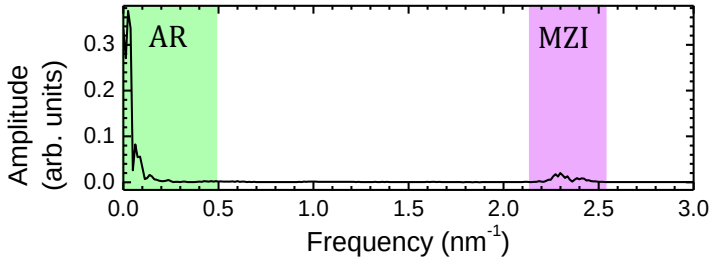

Figure 5.4: FFT spectrum of the 4.0 cm balloon length sensor with respective AR (green) and MZI (lilac) regions.

Such a wide range of bending diameters manifesting MZI makes this sensor more versatile and durable, since smaller bending diameters can compromise the sensor due to higher tension applied on the fiber. Moreover, regardless of the bending diameter, AR guidance will always occur in transmission analysis. When bent under stress the sensor was able to attain the smallest balloon length of 3 cm before breaking. Since the interferometers are enhanced for much longer balloon lengths, the probability of successful sensor preparation is, thus, assured for these lengths.

The capillary length was chosen as a compromise between the MZI visibility, AR visibility, and MZI enhancement. Capillary lengths shorter than 1 cm require smaller balloon bending diameters to enhance the MZI, possibly undermining the integrity of the sensor. Capillary lengths above 1.5 cm have a less defined AR spectrum, making it more difficult to follow the dip during the characterizations.

5.3 Characterization to Pressure

The characterization of the balloons to pressure was done with the closed chamber, the same experimental setup as used in Section 4.4. Since the balloons require a transmission configuration the two ends of the SMF were spliced with two connectors that attach to the two inner entrances on the chamber that, in its turn, connect to the outside of the chamber, with the end of a pigtail connecting to the light source and end of the other pigtail connecting into the OSA.

As seen previously, performing a pressure characterization in SCT-based sensors, an access channel is required in order for pressurized gas to enter the fiber air core. Thus, balloons with an access channel were fabricated and characterized to pressure. As a means to produce a balloon with an access channel, bubbles on the SCT were fabricated according to the process mentioned in Section 4.2. The SCT with a bubble was spliced between two SMFs and the balloon-shape was instituted upon the sensor.

For balloons with varying capillary lengths the response to pressure was found to be the same: closed balloon-like sensors are insensitive to pressure while those with an access channel showcase, for both MZI and AR, a shift towards shorter wavelengths (blue shift), with a superior module for MZI than for AR, as can be seen in Figure 5.5. The pressure sensitivity of the closed balloon-like sensors is of (0.36 ± 0.02) nm/MPa for the MZI and (-0.23 ± 0.03) nm/MPa for the AR, while for open sensors, the attained sensitivities were (-4.7 ± 0.1) nm/MPa for the MZI and (-3.68 ± 0.04) nm/MPa, with high linearity attained ($R^2 \geq 0.899$).

This result aligns with the theoretical predictions, as an increase in pressure results in an increase of the core RI of the SCT, which, according to equations (3.9) and (3.19), leads to a shift towards shorter wavelengths as pressure increases.

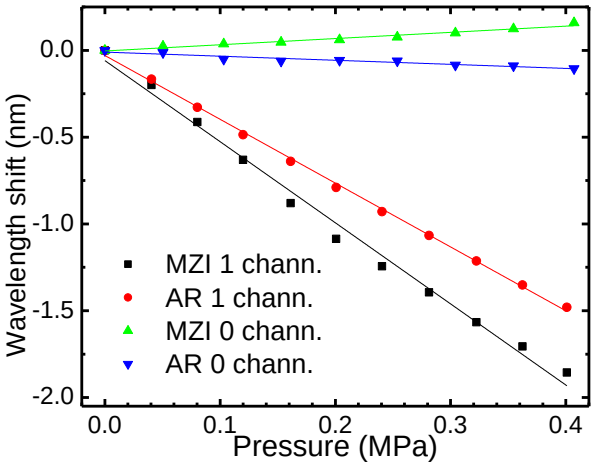

Figure 5.5: Pressure characterization for a balloon with 1 cm length with and without an access channel.

5.4 Characterization to Displacement

The balloon-like sensors (without access channels) were also characterized to other physical parameters. For displacement measurements (setup shown in Figure 5.6) the balloon is placed between two stages and glued with cyanoacrylate at both sides, with the Tygon® tube laying on a base. One stage is fixed while the other is attached to a micrometer screw. Through the screw retraction, the platform moves horizontally, applying an incremental displacement on the balloon, which will become smaller in width and enlarge slightly in length, as shown in Figure 5.8b.

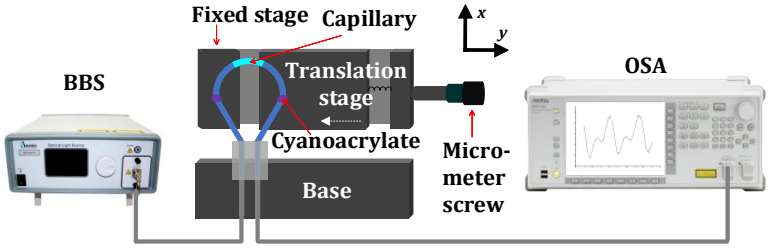

Figure 5.6: Schematic diagram of the displacement setup.

The range of displacement was applied from 0 to 5 mm with steps of 0.25 mm. The dynamic range of these balloon-like sensors is around 20 mm, which is a wider range than previously reported [73]. The displacement response for both interferometers is given in Figure 5.7. The reference points monitored for each interferometer are labeled in Figure 5.3a.

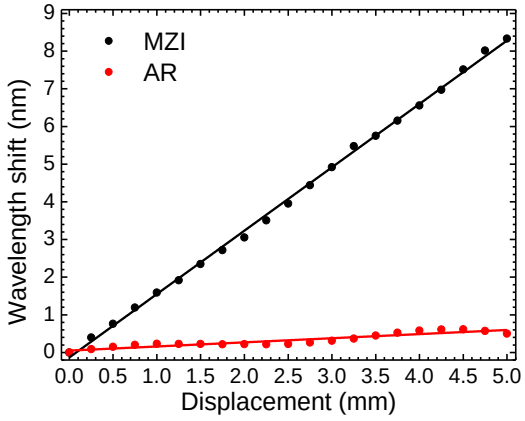

Figure 5.7: Displacement characterization of a balloon with 4 cm length and 1.2 cm capillary length.

The MZI shows a shift towards longer wavelengths (red shift), with a sensitivity of (1.68 ± 0.01) nm/mm, as well as high linearity (R^2 = 0.9986), while the AR component is practically insensitive to displacement with a value of (0.11 ± 0.01) nm/mm and an R^2 of 0.8646.

As the balloon is bent, due to the elasto-optic effect, the RI increases in the extended layer of the bending fiber while for the compressed layer the RI diminishes. The model expressing the RI profile during bending is given by [72]

$$n'(x) = n(x)\left(1 + \frac{x}{r_b}\right), \tag{5.1}$$

where r_b is the bending radius, x is the perpendicular to the bending axis, $n'(x)$ and $n(x)$ are the RI profiles when the sensor is bent and straight, respectively.

As displacement is incrementally applied on the sensor, there is a decrease in the bending radius. Since the core is made of air, the RI will remain mostly the same during displacement increase, while the extended cladding layer will increase in effective RI and the compressed cladding layer will decrease in effective RI [72,74], as shown in Figure 5.8a.

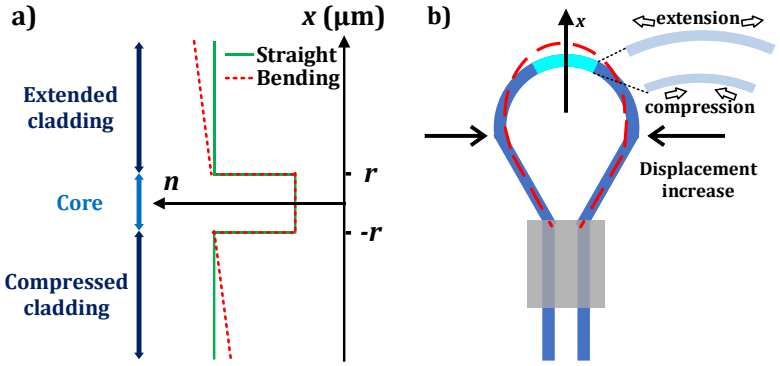

Figure 5.8: (a) RI profile of straight/bending fiber. (b) Schematic diagram of the balloon-like structure with displacement increase.

In this balloon configuration, the MZI only involves the cladding mode of the extended layer and the core mode [75]. According to (3.19), this increase in effective RI will lead to a shift in the transmission. For the AR guidance, this phenomenon occurs for both cladding layers of the SCT, meaning the increase in RI of the extended cladding will be compensated by the decrease in RI of the compressed cladding. Displacement does not affect the cladding thickness, therefore, according to (3.9), the AR is expected to be insensitive to displacement in this balloon configuration.

5.5 Characterization to Temperature

The balloon-like fiber sensors were also characterized to temperature. For this purpose, the sensors were placed on a climatic chamber (Weiss Technik) with controllable temperature and relative humidity, as depicted in Figure 5.9. The initial temperature was set to 15 °C.

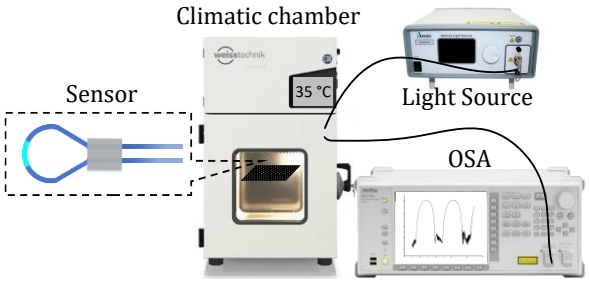

Figure 5.9: Schematic diagram of the temperature setup in the climatic chamber.

After waiting the necessary time to stabilize (around 40 minutes), the spectra were obtained for each sensor with the employment of steps of 2.5 °C within the range of 15 to 35 °C, whilst relative humidity was kept constant at 60% RH. The chamber has an adaptor that allows the pigtails to pass through into the outside of the chamber and connect to the acquisition system.

The temperature response in Figure 5.10 shows that both interferometers are sensitive to this parameter with a red shift. The MZI sensitivity is twice the AR sensitivity, of (28.6 ± 0.1) pm/°C for MZI versus (14.3 ± 0.1) pm/°C for AR. Both results have high linearity with R^2 = 0.9955 and R^2 = 0.9939 for MZI and AR, respectively.

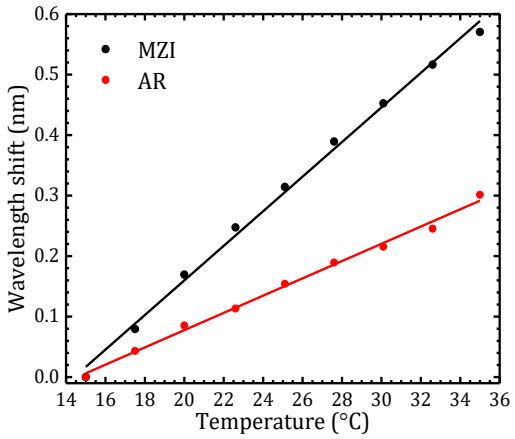

Figure 5.10: Temperature characterization of a balloon with 4 cm length and 1.2 cm capillary length.

The temperature sensitivity of the AR is given by equation (4.14), while that of the MZI is given by

$$\frac{\partial \lambda_{MZI}}{\partial T} = \frac{\Delta n}{m}\frac{\partial L}{\partial T} + \frac{L}{m}\frac{\partial n_2}{\partial T} = \left(\frac{1}{L}\frac{\partial L}{\partial T} + \frac{1}{\Delta n}\frac{\partial n_2}{\partial T}\right)\lambda_{MZI}. \quad (5.2)$$

The TOC of silica is higher than that of air, so as temperature increases, the cladding mode RI will increase more than the RI of the core mode, increasing Δn. Moreover, due to the TEC, an increase in temperature also results in the fiber expanding, increasing the value of L and d. According to the equations (3.19) and (3.9), this results in a positive shift in the transmission spectrum for both MZI and AR. Considering a wavelength peak of $\lambda_{MZI} \approx 1555\ nm$, the theoretical sensitivity of the MZI to temperature is ~30.4 pm/°C, which agrees with the experimentally attained sensitivity. As to the theoretical AR sensitivity, it has already been calculated in section 4.4.3, whose value was of ~26.5 pm/°C. These values are, also, comparable to previously obtained sensitivities in other works [55,76].

The temperature range is limited by the Tygon® tube which is a polymeric material, therefore its TEC is higher than that of silica. As such, it would compromise the sensor response for higher temperatures. Due to the usage of UV glue, a temperature increase results in a change of volume and shape of the glue, interfering with the temperature results. Hitherto, this remains a limitation of this sensor. Replacing the Tygon® capillary with an SCT would grant greater resistance to higher temperatures. Furthermore, the thermal expansion of the tube would no longer be an issue. On the other hand, glue would remain necessary, however a glue with higher temperature resistance could be utilized.

Manifold sensors were developed, and coherent results were achieved in regards to its spectral and characterization results. Both the fabrication and characterization of the sensors showcased high repeatability. The stability of the sensor was assessed by continuously acquiring the sensor spectral response for 30 minutes. A standard deviation of 7 pm and 5 pm was achieved for MZI and AR, respectively, which is within the resolution limits of the OSA.

5.6 Hybrid measurements

Since the sensitivities of the interferometers (MZI and AR) were different for both parameters, this sensor is a good candidate to perform simultaneous measurement of displacement and temperature. A demodulation matrix can be established to calculate the changes of temperature (*T*) and displacement (*D*), which are given by

$$\begin{bmatrix}\Delta\lambda_{MZI}\\ \Delta\lambda_{AR}\end{bmatrix}=\begin{bmatrix}\kappa_{MZI}^{D} & \kappa_{MZI}^{T}\\ \kappa_{AR}^{D} & \kappa_{AR}^{T}\end{bmatrix}\begin{bmatrix}\Delta D\\ \Delta T\end{bmatrix}\Rightarrow\begin{bmatrix}\Delta\lambda_{MZI}\\ \Delta\lambda_{AR}\end{bmatrix}=\begin{bmatrix}1.68 & 0.0286\\ 0.11 & 0.0143\end{bmatrix}\begin{bmatrix}\Delta D\\ \Delta T\end{bmatrix}, \tag{5.3}$$

where $\Delta\lambda$ is the wavelength shift (in nm) and κ_i^j is the sensitivity (in nm/°C or nm/mm). The variation of displacement and temperature can, thus, be expressed in the following matrix

$$\begin{bmatrix}\frac{\Delta D}{\Delta T}\end{bmatrix}=\frac{1}{0.020878}\begin{bmatrix}0.0143 & -0.0286\\ -0.11 & 1.68\end{bmatrix}\begin{bmatrix}\Delta\lambda_{MZI}\\ \Delta\lambda_{AR}\end{bmatrix}. \tag{5.4}$$

Seeing that the MZI reveals greater sensitivity than AR in both measurands, simultaneous measurement of both parameters becomes more difficult when using the matrix method, thus the obtained sensitive cross for this sensor does not reveal perfect perpendicularity and, instead, pertains significant scattering of the experimental results. This limitation is also explained by the low value of the matrix determinant, which induces low precision in simultaneous measurement [77].

From a brief view of the described sensors, in Table 5.1, the continuous growth of balloon-like sensors is clear over the years. As it is a relatively recent discovery, balloon-like sensors have been recurrently used with simple configurations for the detection of parameters. In particular, one would highlight the displacement measurement with great sensitivities and large measuring ranges. The advantage of manipulating and strategically modifying the design of the balloon enables the enhancement of a different set of interferometers, namely FPI, MZI, and ARROW, which can be used to monitor different parameters, further corroborating the versatility of this optical structure.

Table 5.1: Figures of merit of some balloon-like OFS for displacement and temperature measurements.

Year	Sensing structure	Disp. sens. (pm/μm)	Meas. Range (μm)	Temp. sens. (pm/°C)	Hybrid	Ref.
2015	Balloon + FBG	-	-	10.3	Yes (RI)	[78]
2018	Balloon + LPG	-306	0-80	42.9	Yes	[79]
2019	Balloon + FBG	180	0-70	105	Yes	[72]
2019	FBG + balloon + up-tapered MZI	-	-	11	Yes (RH)	[71]
2020	Balloon + core-offset	-528.57	0-120	-31.66	Yes	[80]
2020	2 balloons	-318.8	0-90	47.4	Yes	[75]
2022	Balloon	327.4	0-100	-	No	[74]
2022	Balloon + ARROW	-	-	19	Yes (RI)	[76]
2022	Balloon	71.49	0-800	-	No	[73]
2022	**Balloon (MZI + ARROW)**	**1.68**	**0-5000**	**28.6**	**Yes**	[81]

Note: every balloon structure mentioned in the table (besides [81]) was developed with a bent SMF.

6. Hollow square core fiber hybrid sensor based on FPIs

6.1 Development & Spectral Analysis

Whilst in search for attaining hybrid measurements via development of novel fiber sensing configurations with hollow core fibers, one came across the HSCF as a complex fiber with formidable potential. Heretofore, this fiber, in a sandwich structure, was studied and characterized for several parameters in a transmission configuration [53–55]. In this thesis, however, a similar configuration will be developed and studied in a reflection scheme for a panoply of parameters, namely pressure, temperature, curvature, and strain, achieving a multiparameter application of the former three measurands.

The HSCF used in this work, whose cross-section is shown in Figure 6.1(a,b), is a PCF that contains a square shaped hollow core surrounded by a silica arrangement. This structure is encircled by a silica cladding with a width of ~36.5 µm. The core has a diameter of ~11 µm (2*r*) and the four surrounding air petal-shape structures, intercalated with silica strands of ~1.7 µm of thickness (*w*), extend an internal radius of ~26 µm (*d*), resulting in an outer diameter of 125 µm.

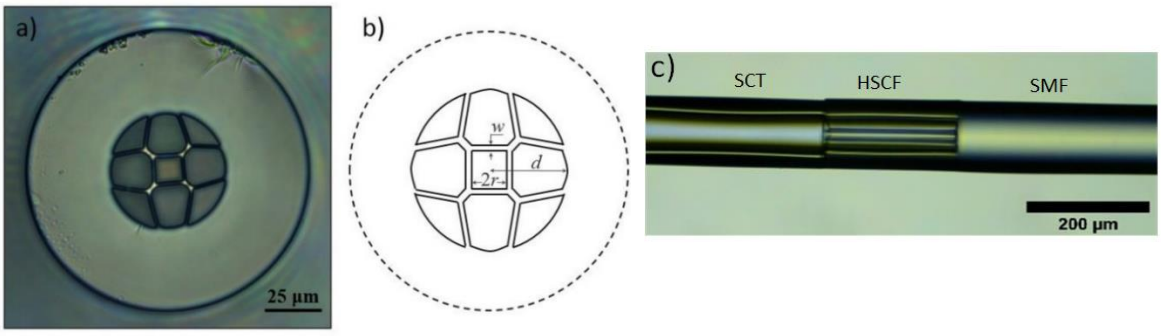

Figure 6.1: (a) Microscopic cross section view of the HSCF. (b) Geometrical scheme of the HSCF [53]. (c) Microscopic view of an SMF-HSCF-SCF configuration.

The sensor design was developed with a short section of the HSCF spliced with an SMF and with a long section of SCT that has a 57 µm inner diameter, as seen in Figure 6.1c. The parameters for the splice in question were, in the manual mode, 12 bits of power and 500 ms of arc discharge time, with the offset technique described in section 4.1, thus preserving the fiber microstructures by minimizing the collapsing of its inner arrangements. A longer arc discharge would result in a collapse of the external cladding whilst damaging the internal structure. Nonetheless, a slight collapse can be seen in the HSCF-SCT splice. This configuration possesses an air cavity for pressure detection, located in the air core of the HSCF, and the sensor has sufficient length for a strain and curvature characterization. This was ensured by the portion of SCT, which acts as an input gas channel and as a support structure for the characterization of physical parameters.

In a reflection scheme, the spectra of sensors in this configuration were obtained for different lengths as shown in Figure 6.2. Firstly, in a 121 µm sensor, a two-wave interferometer can be observed, corresponding to an FPI created in the SMF-HSCF interface and the HSCF-SCT interface, which is evidenced in a sharp peak of this sensor FFT spectrum. Now, as the HSCF length increases, the enhancement of more modes occurs wherein light couples to different areas of the fiber and recouples back to the SMF. As seen in a 224 µm sensor, two distinct modes can be observed in the FFT spectrum with nearby frequencies, leading one to assume that these arise from several excited

FP cavities in the fiber. This is facilitated by the dimensions of the hollow core of the fiber as the HSCF has a diameter close to that of the SMF. Additionally, a modulation in the sensors reflection spectra is evidenced which results in beats between the two highest frequencies. In the FFT spectrum, the beat phenomenon corresponds to the low frequency, low amplitude peak in the 0.02-0.05 m^{-1} range. Finally, for a 439 µm long sensor, several harmonic oscillations with nearby frequencies occur in the reflection spectrum, as evidenced by the three distinct resonant peaks in the FFT spectrum that correspond to the enhancement of three different FP cavities in the HSCF. When the HSCF has a length above 600 µm, its FFT spectrum is increasingly more complex, and peaks become less defined. Thus, the optimal length where three FP cavities are excited was found to be within the 250-600 µm region.

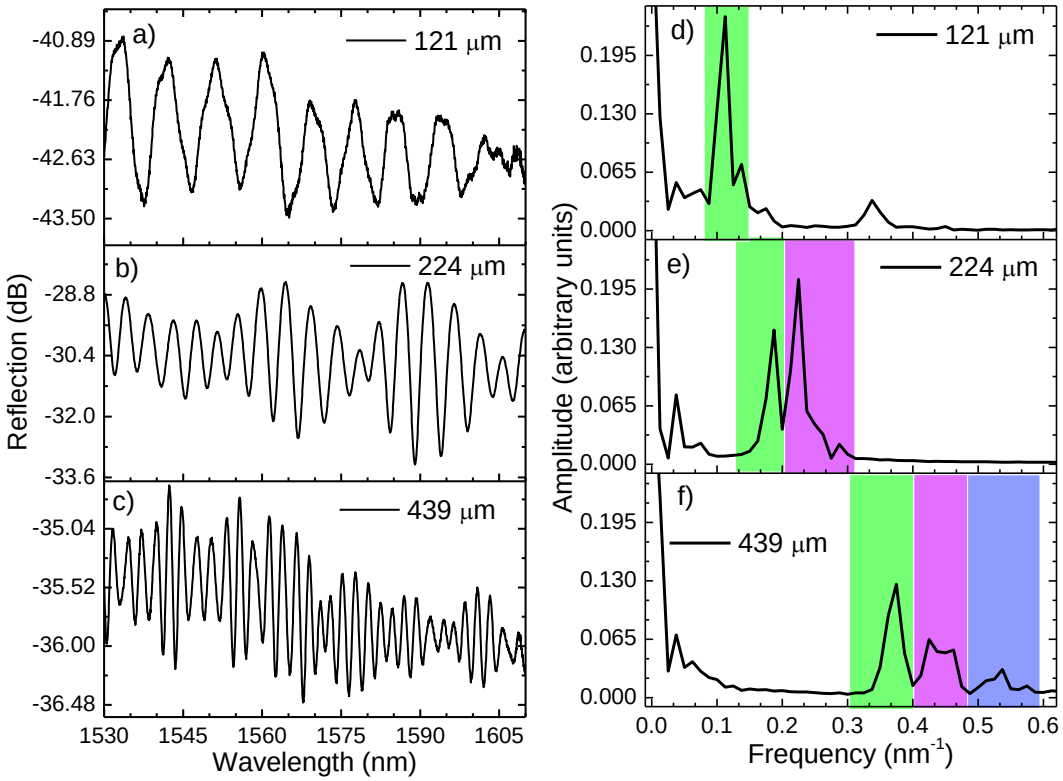

Figure 6.2: Spectrum (a-c) and respective FFT (d-f) of HSCF sensors with different lengths. Fourier band pass filter (FPBF) regions were highlighted for the visible modes, resultant from excited cavities in the sensor.

It can, then, be concluded that the longer the HSCF length, the more FP cavities are excited, but the lower the visibility of the reflection spectra. Moreover, a decrease in the FSR of the FPIs occurs, and a more complex FFT spectrum arises. It is, also, noteworthy that in the second interface, HSCF-SCT, there are mirrors with miniature dimensions which correspond to the silica strands.

By using the Fourier band pass filtering (FBPF) method to process the original spectrum, the different FP cavities can be discerned, greatly reducing the error caused by the inconsistency of the wavelength shift of 2 different dips with close frequencies. The application of this method with a specific frequency range allows the fringe spectral discrimination of each cavity, removing the contributions of the other cavities due to a smart frequency selection for the filter. This method can be employed to analyze the specific FPI, does not depend on the specific dip wavelength tracked, and helps reducing the effects of the other FPIs [40,52,65]. A multiple-dip tracing technique and the FBPF method is, therefore, serviceable towards multiparameter measurements.

Due to imperfections in the fiber and the splice quality, an easy peak selection from the FFT spectrum becomes a hindrance where longer sensors are concerned, as crosstalk between the cavities can occur during the filtering process. Thus, a compromise of the sensing length must be made in order to enhance 3 FPIs whilst enabling a non-inconspicuous filtering selection.

For the 439 µm sensor, the three resonance peaks are easy to discern in the FFT spectrum as seen in Figure 6.2f with the regions in green, lilac, and blue for the first, second, and third modes, respectively. Thus, three band-pass filters were applied so as to obtain the interference of each FP cavity with the following frequencies: 0.30 – 0.40 nm^{-1}, 0.40 – 0.49 nm^{-1} and 0.49 – 0.60 nm^{-1}, whose results are shown in Figure 6.3.

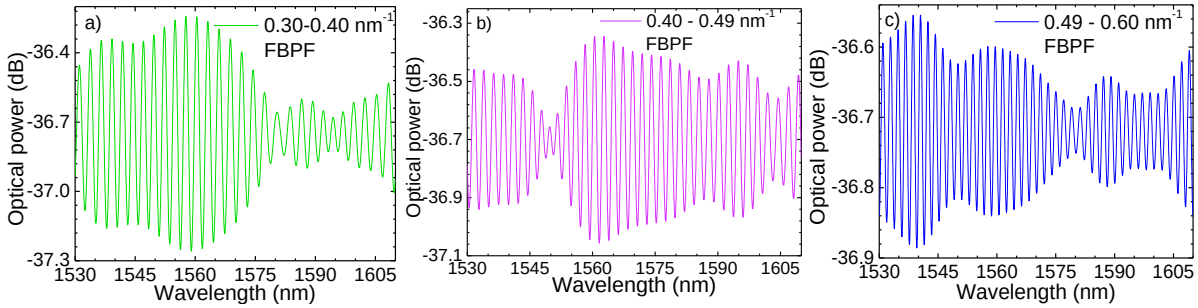

Figure 6.3: FBPF spectral results for each FP cavity excited in the 439 µm HSCF sensor.

Initially, SMF-HSCF fiber-tip sensors were developed for pressure and temperature detection. Though, the enhancement of 3 FPIs put forth a potential multiparameter application for the detection of physical measurands, thus a splice with an SCT was introduced for this purpose. Both configurations were plotted regarding their FSR in relation to the HSCF length, as show in Figure 6.4a. It is clear that an inversely proportional dependence is verified, equally for the configurations with and without the SCT. Furthermore, the results attained are coherent for both structures, corroborating the fact that the introduction of an SCT does not have a significant impact on the effective RIs of the modes. Furthermore, in order to determine an effective RI average, a linearization based on equation (3.5) was proposed for the original spectrum and each mode of the sensors with an SCT:

$$\Delta\lambda = \frac{\lambda^2}{2n_{eff}}\frac{1}{L}. \tag{6.1}$$

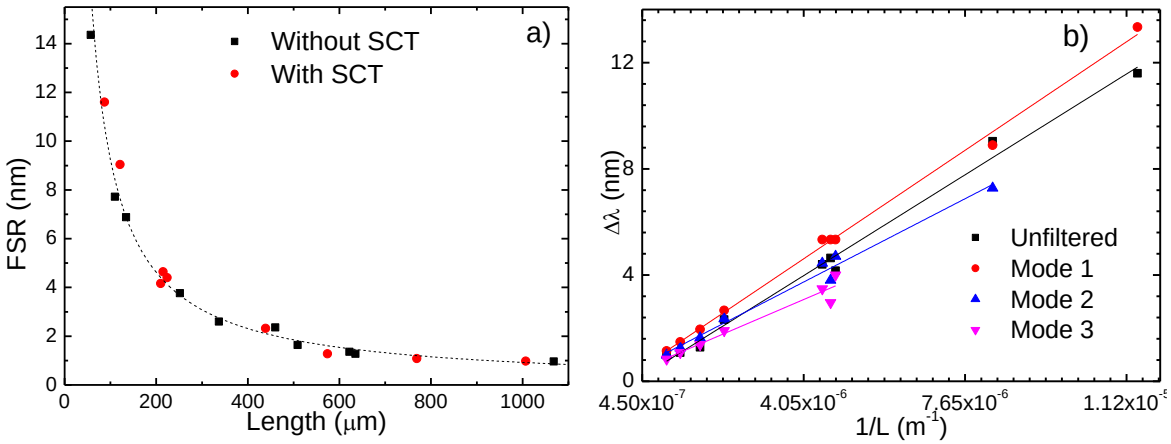

Figure 6.4: (a) FSR vs Length. (b) Plotted FSR vs 1/L for several sensor lengths for each mode.

The value *L* was measured by the microscopic images with aid of the ImageJ software tool. Thus, the effective RI of each mode is given by $\lambda^2/2m$ where *m* is the slope of the linear fit depicted in Figure 6.4b. Interpreting the results presented in Table 6.1, one would infer that the first mode occurs primarily in the air due to the effective RI being close to 1, while the second mode is near the RI of silica, with the third mode possessing an effective RI that does not hold physical meaning as it is greater than that of silica, which could be related with FFT analysis due to resolution limitations in the spectrum itself. Additionally, this result could be related with a harmonic of one of the modes or the group velocity of the cavity. In order to further corroborate the previous statements, a larger number of sensors with varying lengths would have to be fabricated that enhance multiple FPIs.

Table 6.1: Calculated effective RI for each mode of the HSCF.

Filters	Effective RI
Unfiltered	1.14 ± 0.04
Mode 1	1.06 ± 0.02
Mode 2	1.38 ± 0.07
Mode 3	1.6 ± 0.2

In Figure 6.5, three different simulated modes are presented for the silica strands in the HSCF which represent hypothetical locations in the fiber whereat the FP cavities might be enhanced. It is, however, required to perform further studies in this regard so as to obtain logical conclusions. This study falls outside of the scope of this thesis, being proposed as a future work.

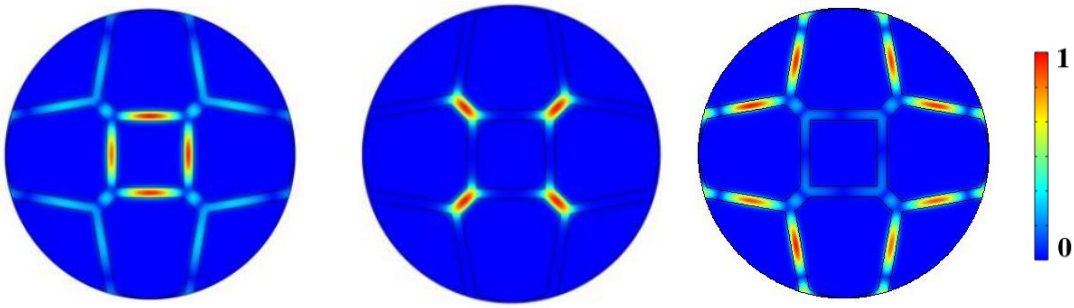

Figure 6.5: Some simulated silica strand modes in the HSCF by using the COMSOL Multiphysics [55].

6.2 Characterization for multiparameter sensing

The presence of three different FP cavities brings about the potential for multiparameter sensing whereby two or more parameters can be detected simultaneously and independently. On the condition that each FPI possesses different sensitivities for each parameter in study, a multiple-hybrid application can be readily achieved via the FBPF method. Apropos to this, a characterization to several physical parameters was performed for the HSCF in a reflection scheme. Although all sensors were characterized towards each parameter below presented for comparison purposes, the focus will be on the sensors that enhance three modes, as they possess the most promising application for simultaneous measurement of three parameters.

6.2.1 Pressure

The pressure measurements were carried out by resorting to the experimental setup used in Section 4.4.1. The experimental results attained for a 439 µm sensing head are represented in Figure 6.6 where it is visible that the three components are sensitive to pressure. For the filters, a red shift is observed, with the lower frequency interferences presenting higher sensitivity to pressure. The attained sensitivities to pressure were, for modes 1, 2 and 3, (3.23 ± 0.04) nm/MPa, (2.03 ± 0.01)

nm/MPa, and (0.86 ± 0.01) nm/MPa, respectively, with high linearity ($R^2 \geq 0.99888$) evidenced for all results.

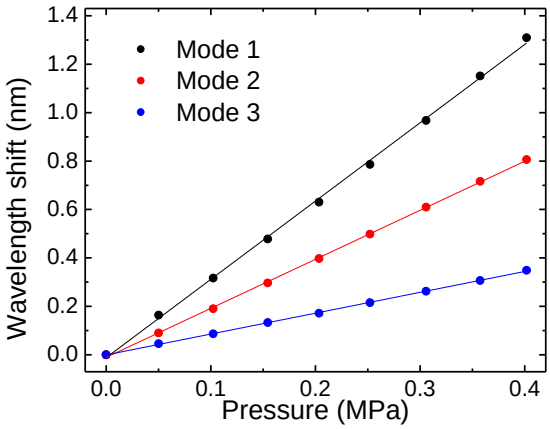

Figure 6.6: Pressure characterization of an HSCF with 439 µm for each FBPF.

The attained results are related with the propagating areas of the modes. As mode 1 presents a lower effective RI, it is more influenced by the dependence of the air RI with pressure. Notice that the sensitivity obtained is close to the one achieved by the hybrid sensor described in Chapter 4. On the other hand, for modes with higher frequency, their RI is closer to that of silica, thus the change in the structure that composes the cavity becomes dominant, decreasing the sensitivity.

6.2.2 Temperature

The characterization of the sensors to temperature was conducted in the experimental setup used in Section 5.5. The temperature range applied, however, was greater, varying from 20 to 110 °C since the sensor is constituted only of silica which can withstand temperatures as high as 1000 °C [82]. Consequently, the temperature range is only limited by the climatic chamber. The experimental results obtained are given in Figure 6.7. The obtained sensitivities to temperature were (2.9 ± 0.2) pm/°C, (6.6 ± 0.2) pm/°C, and (9.6 ± 0.3) pm/°C, for the first, second, and third modes, respectively, with high linearity ($R^2 \geq 0.977$) attained for all modes.

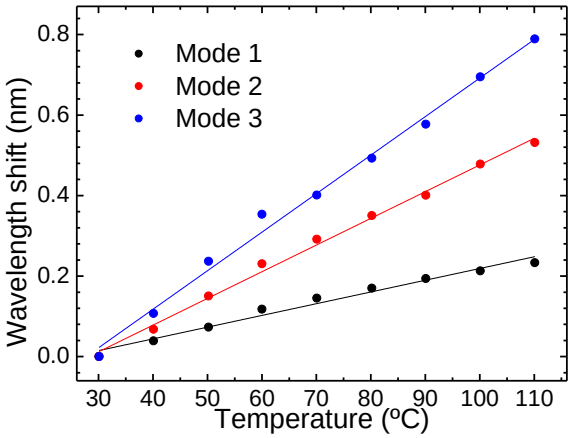

Figure 6.7: Temperature characterization of an HSCF with 439 µm for each FBPF.

Although the shift in the filter response is towards longer wavelengths, contrary to the behavior of the pressure response, it is the higher frequencies that showcase greater sensitivity to temperature. This is also expected when considering a descriptive model based on the effective RI of each mode as silica-based FPIs present higher temperature sensitivity than the ones composed of air [17].

6.2.3 Strain

The strain measurements were performed in a setup given in Figure 6.8, in which the sensor is displaced between a fixed stage and a translation stage, distanced 17 cm from one another. The translation stage moves horizontally away from the fixed stage, thus applying strain on the sensor. The strain characterization was carried out by stretching the fiber to a total elongation of 110 µm, in steps of 10 µm, corresponding to a maximum strain of ~650 µε.

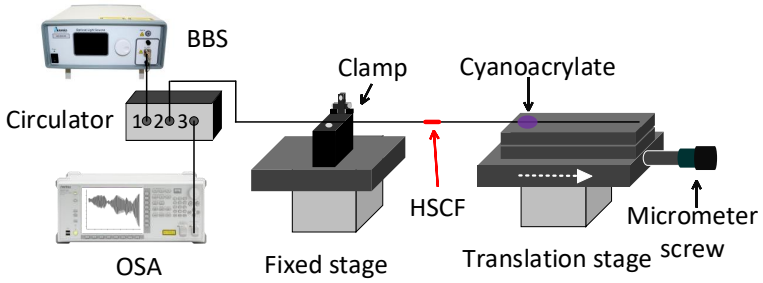

Figure 6.8: Schematic diagram of the strain experimental setup.

The experimental results are presented in Figure 6.9. As was verified in the pressure response, the shift in the filter spectra is towards longer wavelengths, bestowing a higher sensitivity to strain the interferences with lower frequency. The first mode reveals a sensitivity of (1.26 ± 0.03) pm/µε, the second mode possesses a sensitivity of (1.07 ± 0.02) pm/µε, and the third mode has a sensitivity of (0.85 ± 0.01) pm/µε to strain, with great linearity ($R^2 \geq 0.99416$) showcased for all mode responses.

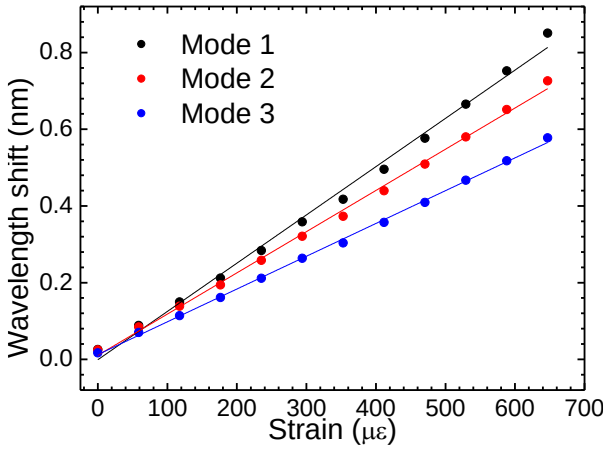

Figure 6.9: Strain characterization of an HSCF with 439 µm for each FBPF.

Notice that the sensitivities obtained are lower than the ones usually reported in literature for inline FPIs [51]. This is attributed to the fact that the strands are not spliced to the SCT since this capillary has a diameter greater than that of the HSCF silica structure. Thus, the strands will not suffer the same elongation as the whole fiber structure. Furthermore, the lower sensitivities observed for higher frequencies can, once again, be attributed to the higher effective RIs.

In order to fulfill a multiparameter application, the utilization of the matrix method described previously is fundamental. Yet, certain criteria must be verified. Specifically, with respect to the strain and pressure characterizations, the cavities have similar responses, therefore attaining an impediment for the measurement of both parameters in an independent manner. Thus, a new parameter was suggested that could potentially overcome this conundrum: curvature.

6.2.4 Curvature

The curvature experimental apparatus is similar to Figure 6.8 apart from the platform translation direction, which was done towards the fixed stage, inducing a bending on the sensor. Additionally, a rotational clamp was connected to a fiber holder that is attached to the fixed stage, as shown in Figure 6.10, thus directional bending can be performed by performing curvature experiments for a certain direction imposed by the clamp rotation. The curvature (C) subjected upon the sensor can be determined by [55]

$$C = R^{-1} = \frac{2h}{h^2 + D^2}, \tag{6.2}$$

where *2D* is 17.3 cm, corresponding to the distance between the glued points wherein the sensor is fixed, *h* is the height of the sensor center in relation to the horizontal plane, and *R* is the radius of the sensor bending. For the characterization of the sensor, a maximum height of 40 mm was achieved in bending with steps of 2 mm, which corresponds to an approximate value of total curvature of 9 m^{-1}. The curvature experiment was repeated within a rotation range of [-270°,270°] with steps of 90°.

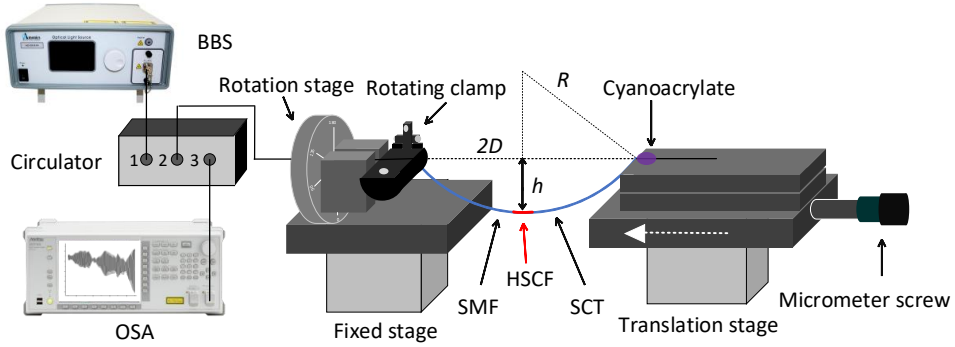

Figure 6.10: Schematic diagram of the curvature experimental setup.

The experimental results are represented in Figure 6.11. One draws attention to the different responses of the filters, namely a shift towards longer wavelengths for some modes and a shift towards shorter wavelengths for others, which is quite a distinct response from previous characterizations.

As depicted in the multiple curvature responses given in Figure 6.11, it is clear that the sensor can provide directional/vector bending detection due to the varying responses of the modes as curvature is induced in the fiber for different fiber positions, imposed by the rotation clamp. When the rotation direction is negative, mode 1 has a negative sensitivity to curvature and mode 2 and 3 showcase a shift towards longer wavelengths, with greater sensitivity revealed by the third mode. For a positive rotation direction, the behavior is symmetrical. The attained sensitivities are summarized in Table 6.2 and illustrated in Figure 6.12.

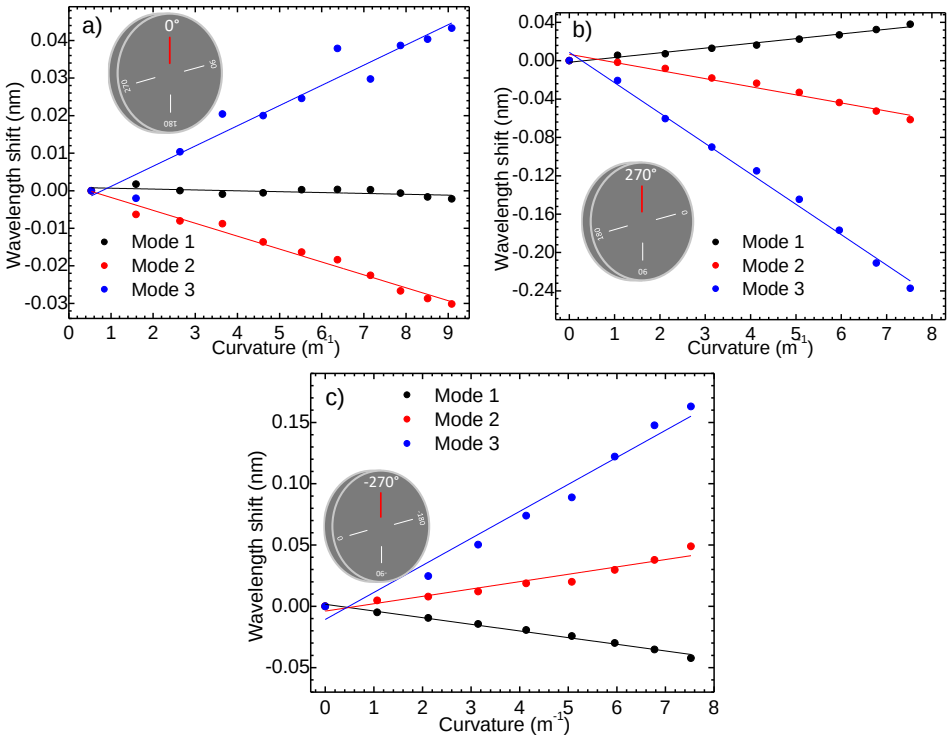

Figure 6.11: Curvature characterization of the HSCF at (a) 0°, (b) 270°, and (c) -270°.

Table 6.2: Bending sensitivities for a certain rotation.

Rot. (°)	κ_1 (pm/m^{-1})	κ_2 (pm/m^{-1})	κ_3 (pm/m^{-1})
-270	-5.4 ± 0.2	6.0 ± 0.6	22 ± 1
-180	-6.3 ± 0.2	3.9 ± 0.3	20 ± 2
-90	-4.8 ± 0.1	0.9 ± 0.2	12.7±0.5
0	-0.2 ± 0.1	-3.4 ± 0.2	5.4 ± 0.5
90	4.1 ± 0.1	-6.8 ± 0.2	-11.8±0.7
180	5.4 ± 0.2	-8.4 ± 0.1	-24 ± 1
270	4.9 ± 0.3	-8.5 ± 0.6	-32 ± 1

Though the sensitivities are not completely equal in module for symmetric rotations, they still follow a coherent behavior consistently throughout the different bending directions. The coefficient of determination for the results is comprised between $R^2 \in [0.922, 0.995]$.

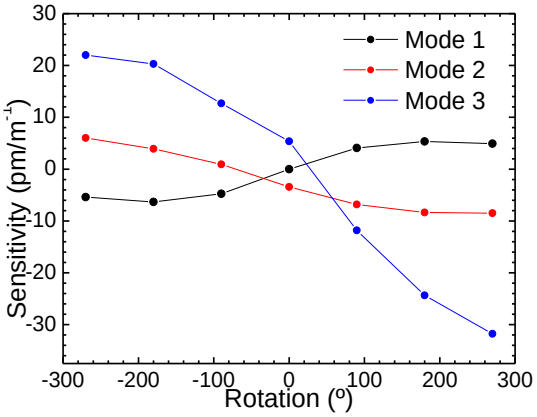

Figure 6.12: Curvature sensitivity of the HSCF at different sensitivities.

When bending is thrusted upon the fiber, a compression of one side of the fiber and the extension of the other side will occur, delimited by a neutral bending plane where no strain is applied. The elasto-optic effect, as explained in section 5.4 will lead to a change in RI of the material, resulting in the different responses given by the modes in the HSCF. The highly complex behavior of this sensor will require computational simulations (e.g. with Solidworks) to better understand the impact each component (rotation and curvature) has in each FPI. This study is outside the scope of this thesis and is proposed as a future work. Still, as an experimental proof-of-concept, this parameter shows high potential to be combined with two of the other parameters previously studied.

6.2.5 Simultaneous measurement of pressure, temperature, and curvature

The results achieved reveal a possible hybrid application of the sensor towards the simultaneous detection of the studied parameters. The experimental setups for curvature and strain were identical, with the fiber being displaced in opposite directions, thus the simultaneous measurement of these parameters is not relevant since the configuration at hand disables the fiber from exerted strain while curvature is instilled. Therefore, the simultaneous measurement of pressure (*P*), temperature (*T*), and curvature (*C*) will be carried out. The distinct responses that the FP cavities present to each measurand can be described by the following matrix:

$$\begin{bmatrix}\Delta\lambda_1\\ \Delta\lambda_2\\ \Delta\lambda_3\end{bmatrix}=\begin{bmatrix}\kappa_{P,1} & \kappa_{T,1} & \kappa_{C,1}\\ \kappa_{P,2} & \kappa_{T,2} & \kappa_{C,2}\\ \kappa_{P,3} & \kappa_{T,3} & \kappa_{C,3}\end{bmatrix}\begin{bmatrix}\Delta P\\ \Delta T\\ \Delta C\end{bmatrix}, \tag{6.3}$$

where the variable $\kappa_{i,j}$ stands for the sensitivity of the studied measurand, i, of the corresponding sensing cavity, j. Considering the polar opposite rotations (270° and -270°) and substituting the sensitivities with the respective values one can acquire the direct parameter variation according to the wavelength shifts verified on the sensor:

$$\begin{bmatrix}\Delta P\\ \Delta T\\ \Delta C_{-270^\circ}\end{bmatrix}=\begin{bmatrix}3.23 & 0.0029 & -0.006\\ 2.03 & 0.0066 & 0.00731\\ 0.86 & 0.0096 & 0.0245\end{bmatrix}^{-1}\begin{bmatrix}\Delta\lambda_1\\ \Delta\lambda_2\\ \Delta\lambda_3\end{bmatrix}, \tag{6.5a}$$

$$\begin{bmatrix}\Delta P\\ \Delta T\\ \Delta C_{270^\circ}\end{bmatrix}=\begin{bmatrix}3.23 & 0.0029 & 0.0049\\ 2.03 & 0.0066 & -0.0085\\ 0.86 & 0.0096 & -0.032\end{bmatrix}^{-1}\begin{bmatrix}\Delta\lambda_1\\ \Delta\lambda_2\\ \Delta\lambda_3\end{bmatrix}. \tag{6.5b}$$

Note that the units of ΔP, ΔT, ΔC, and $\Delta\lambda$ are MPa, °C, m^{-1}, and nm, respectively. This outcome reveals a potential application of this sensor in the simultaneous measurement of these parameters, with the assumption that rotation is fixed at a certain value. Thus, in a single sensing element, with a simple configuration, this sensor is able to achieve triple-hybrid detection, merely resorting to monitoring FPIs via the FBPF method, making it an outstanding candidate for numerous applications. Namely, it is proposed the implementation of this sensor in the aerospace industry where harsh conditions are present, and the detection of various physical parameters with high precision is required.

7. Conclusion and future work

In this work, three hybrid OFSs based on HCFs were successfully implemented. The enhancement of multiple interferometers in one sensing cavity was conducive to a multiparameter detection application. Firstly, the critical length behavior was explored for the enhancement of the AR guidance in a SCT spliced between two SMFs, and a study was conducted on the criteria towards the enhancement of an FPI and an MZI in the same structure.

The first hybrid sensor designed is based on a section of SCT with access channels. Two different methods were developed which allow the fabrication of a sensor with up to two access channels. These sensors were studied in a reflection configuration that revealed FPI and AR phenomena. Both interferometers were monitored and characterized to variations of pressure and temperature for sensors with 2 mm and with 0, 1, and 2 access channels. For pressure, sensitivities of (4.09 ± 0.01) nm/MPa and (-3.7 ± 0.1) nm/MPa were obtained for the FPI and AR, respectively in a sensor with 1 access channel, while for temperature, the highest sensitivities of (-0.39 ± 0.05) pm/°C and (20.17 ± 0.05) pm/°C were respectively achieved for the FPI and AR were revealed in a 2 access channel sensor. The pressure flow established in a 2 access channel sensor resulted in a smaller sensitivity of AR. According to the sensor output matrix, a maximum resolution of ± 2.6×10^{-4} MPa and ± 2.6 °C were attained for pressure and temperature, respectively.

In a different configuration, balloon-like fiber sensors were developed and characterized to pressure, temperature, and displacement and a simultaneous measurement of the latter two parameters was achieved. These sensors are based on an SMF-SCT-SMF structure that is bent in a balloon-like shape, with the SCT at the top-center position of the balloon. In a sensor with 1.2 cm SCT length and 4 cm balloon-length, not only is there AR guidance present, but also an MZI was enhanced in a transmission configuration due to the bending derived from the balloon structure. The simultaneous measurement of displacement and temperature was achieved with the highest sensitivities obtained of (1.68 ± 0.01) nm/mm and (0.11 ± 0.01) nm/mm in displacement and (28.6 ± 0.1) pm/°C and (14.3 ± 0.1) pm/°C in temperature for the MZI and AR, respectively. An access channel was instilled on the SCT for pressure detection, with an obtained sensitivity of (-4.7 ± 0.1) nm/MPa and (-3.68 ± 0.03) nm/MPa for MZI and AR, respectively.

Finally, a multiparameter study was developed for a HSCF sensor with a length of 439 µm. The sensor possessed a configuration based on a SMF-HSCF-SCT in a reflection scheme, that was able to excite up to three distinct FP cavities in a single sensing element. This sensor was monitored towards variations of pressure, temperature, strain, and directional bending. In order to obtain the distinct response of each mode, a FBPF was applied that allows independent mode monitoring with reduced crosstalk. For pressure characterization, the highest sensitivity of (3.23 ± 0.04) nm/MPa was attained for the first mode, with decreasing sensitivity for higher frequency modes. The maximum temperature sensitivity obtained was (9.6 ± 0.3) pm/°C for the third mode, with decreasing sensitivity for lower frequency modes. For the strain characterization, a similar response to the pressure detection was observed, with the highest attained sensitivity of (1.26 ± 0.03) pm/µε for mode 1. As to directional bending, a curvature experiment was performed for several bending directions with symmetrical results obtained for positive and negative rotations. Considering a rotation of 270°, sensitivities of (4.9 ± 0.2) pm/m^{-1}, (-8.2 ± 0.4) pm/m^{-1}, and (-32 ± 1) pm/m^{-1} were obtained for the first, second and third modes, respectively. The different mode responses for

pressure, temperature, and curvature were conducive to a multiparameter triple-hybrid simultaneous measurement of these parameters.

For future work, a simulation of the strain and stress profiles of the access channel-based fiber sensor is proposed towards one and two access channel configurations. This simulation could explain the varying AR sensitivities to pressure when a sensor with 1 or 2 access channels is studied. Furthermore, a more detailed study is proposed for the optimum length of the balloon as well as the capillary length to achieve a higher sensitivity to displacement. A simulated model of the HSCF reflection modes is, also, proposed that could better understand the enhancement of the previously studied FP cavities. The proposed computational simulation could discriminate where the different modes, observed in reflection, propagate in the HSCF.

The detection of gases is proposed for the access channel-based sensors. Particularly, towards volatile organic compounds, which are chemical compounds with high steam pressure at room temperature. Additionally, coating the sensor with an adequate polymer that could enhance sensitivity is proposed.

At last, it is also intended to further extend the study on hybrid interferometric fiber sensor by exploring other fiber structures and configurations towards simultaneous multiparameter detection.

Bibliography

[1] B. Culshaw, “City of light — the story of fibre optics,” *Opt Lasers Eng*, vol. 33, no. 1, 2000, doi: 10.1016/s0143-8166(00)00008-7.

[2] R. Tricker, “The history of fiber optics,” in *Optoelectronics and Fiber Optic Technology*, 2002. doi: 10.1016/b978-075065370-1/50003-9.

[3] John M. Senior, *Optical Fiber Communications Principles and Practice Third Edition*. 2009.

[4] S. Kumar and M. J. Deen, *Fiber optic communications: Fundamentals and applications*, vol. 9780470518670. 2014. doi: 10.1002/9781118684207.

[5] B. Lee, “Review of the present status of optical fiber sensors,” *Optical Fiber Technology*, vol. 9, no. 2, 2003, doi: 10.1016/S1068-5200(02)00527-8.

[6] F. T. S. Yu and S. Yin, *Fiber optic sensors*. Marcel Dekker, 2002.

[7] G. D. Pitt *et al.*, “Optical-fiber sensors.,” *IETE Technical Review (Institution of Electronics and Telecommunication Engineers)*, vol. 3, no. 8, 1986, doi: 10.1080/02564602.1986.11438006.

[8] A. Bornstein and N. Croitoru, “Experimental evaluation of a hollow glass fiber,” *Appl Opt*, vol. 25, no. 3, 1986, doi: 10.1364/ao.25.000355.

[9] M. A. Duguay, Y. Kokubun, T. L. Koch, and L. Pfeiffer, “Antiresonant reflecting optical waveguides in SiO2-Si multilayer structures,” *Appl Phys Lett*, vol. 49, no. 1, 1986, doi: 10.1063/1.97085.

[10] J. F. Giuliani, H. Wohltjen, and N. L. Jarvis, “Reversible optical waveguide sensor for ammonia vapors,” *Opt Lett*, vol. 8, no. 1, 1983, doi: 10.1364/ol.8.000054.

[11] B. H. Weigl, O. S. Wolfbeis, and B. H. Weigl, “Capillary Optical Sensors,” *Anal Chem*, vol. 66, no. 20, 1994, doi: 10.1021/ac00092a007.

[12] O. S. Wolfbeis, “Capillary waveguide sensors,” *TrAC - Trends in Analytical Chemistry*, vol. 15, no. 6, 1996, doi: 10.1016/0165-9936(96)85131-4.

[13] P. S. J. Russell, “Photonic-crystal fibers,” *Journal of Lightwave Technology*, vol. 24, no. 12, 2006, doi: 10.1109/JLT.2006.885258.

[14] W. Ni *et al.*, “Recent advancement of anti-resonant hollow-core fibers for sensing applications,” *Photonics*, vol. 8, no. 4. 2021. doi: 10.3390/photonics8040128.

[15] J. Santos and F. Farahi, *Handbook of Optical Sensors*. 2014. doi: 10.1201/b17641.

[16] R. di Sante, “Fibre optic sensors for structural health monitoring of aircraft composite structures: Recent advances and applications,” *Sensors (Switzerland)*, vol. 15, no. 8. 2015. doi: 10.3390/s150818666.

[17] S. Pevec and D. Donlagić, “Multiparameter fiber-optic sensors: a review,” *Optical Engineering*, vol. 58, no. 07, 2019, doi: 10.1117/1.oe.58.7.072009.

[18] Y. Zhang, J. Huang, X. Lan, L. Yuan, and H. Xiao, “Simultaneous measurement of temperature and pressure with cascaded extrinsic Fabry–Perot interferometer and intrinsic Fabry–Perot interferometer sensors,” *Optical Engineering*, vol. 53, no. 6, 2014, doi: 10.1117/1.oe.53.6.067101.

[19] S. Pevec and D. Donlagic, “Miniature all-fiber Fabry-Perot sensor for simultaneous measurement of pressure and temperature,” *Appl Opt*, vol. 51, no. 19, 2012, doi: 10.1364/AO.51.004536.

[20] S. Pevec and D. Donlagic, “Miniature fiber-optic sensor for simultaneous measurement of pressure and refractive index,” *Opt Lett*, vol. 39, no. 21, 2014, doi: 10.1364/ol.39.006221.

[21] Z. Ran, C. Li, H. Zuo, and Y. Chen, “Laser-machined cascaded micro cavities for simultaneous measurement of dual parameters under high temperature,” *IEEE Sens J*, vol. 13, no. 5, 2013, doi: 10.1109/JSEN.2013.2241537.

[22] S. Pevec and D. Donlagic, “High resolution, all-fiber, micro-machined sensor for simultaneous measurement of refractive index and temperature,” *Opt Express*, vol. 22, no. 13, 2014, doi: 10.1364/oe.22.016241.

[23] Y. Liu, B. Li, X. Song, D. Yang, and Y. Wang, “FPI-based fibre-optic sensor fabricated by excimer laser micromachining and fusion splicing HCF for multi-parameter measurements,” *J Mod Opt*, vol. 67, no. 15, 2020, doi: 10.1080/09500340.2020.1842927.

[24] S. Pevec and D. Donlagic, “MultiParameter fiber-optic sensor for simultaneous measurement of thermal conductivity, pressure, refractive index, and temperature,” *IEEE Photonics J*, vol. 9, no. 1, 2017, doi: 10.1109/JPHOT.2017.2651978.

[25] H. Luo, Q. Sun, Z. Xu, W. Jia, D. Liu, and L. Zhang, “Microfiber-based inline Mach-Zehnder interferometer for dual-parameter measurement,” *IEEE Photonics J*, vol. 7, no. 2, 2015, doi: 10.1109/JPHOT.2015.2395133.

[26] Y. Chen *et al.*, “A Hybrid Multimode Interference Structure-Based Refractive Index and Temperature Fiber Sensor,” *IEEE Sens J*, vol. 16, no. 2, 2016, doi: 10.1109/JSEN.2015.2484346.

[27] Q. Wu, Y. Semenova, P. Wang, and G. Farrell, “Fibre heterostructure for simultaneous strain and temperature measurement,” *Electron Lett*, vol. 47, no. 12, 2011, doi: 10.1049/el.2011.0974.

[28] J. Harris, P. Lu, H. Larocque, Y. Xu, L. Chen, and X. Bao, “Highly sensitive in-fiber interferometric refractometer with temperature and axial strain compensation,” *Opt Express*, vol. 21, no. 8, 2013, doi: 10.1364/oe.21.009996.

[29] N. Zhang *et al.*, “Simultaneous measurement of refractive index, strain and temperature using a tapered structure based on SMF,” *Opt Commun*, vol. 410, 2018, doi: 10.1016/j.optcom.2017.09.096.

[30] X. Gao *et al.*, “Simultaneous measurement of refractive index, strain, and temperature based on a Mach–Zehnder interferometer with hybrid structure optical fiber,” *Appl Opt*, vol. 58, no. 30, 2019, doi: 10.1364/ao.58.008187.

[31] M. Wu *et al.*, “Mach-Zehnder interferometer for multi-parameter measurement sensor based on SMF-NCF-FMF-NCF-SMF,” *Optik (Stuttg)*, vol. 249, 2022, doi: 10.1016/j.ijleo.2021.168227.

[32] Y. Zhao, X. G. Li, L. Cai, and Y. N. Zhang, “Measurement of RI and Temperature Using Composite Interferometer with Hollow-Core Fiber and Photonic Crystal Fiber,” *IEEE Trans Instrum Meas*, vol. 65, no. 11, 2016, doi: 10.1109/TIM.2016.2584390.

[33] Y. Wu *et al.*, “Fiber optic hybrid structure based on an air bubble and thin taper for measurement of refractive index, temperature, and transverse load,” *Optik (Stuttg)*, vol. 241, 2021, doi: 10.1016/j.ijleo.2021.166962.

[34] B. Su, B. Qi, F. Zhang, L. Zhong, O. Xu, and Y. Qin, “Hybrid Fiber Interferometer Sensor for Simultaneous Measurement of Strain and Temperature with Refractive Index Insensitivity,” *SSRN Electronic Journal*, 2022, doi: 10.2139/ssrn.4063136.

[35] W. Zhou, C. L. Zhao, J. Huang, and X. Dong, “A novel FBG sensing head geometry for strain-temperature discrimination,” in *2009 Asia Communications and Photonics Conference and Exhibition, ACP 2009*, 2009. doi: 10.1117/12.851312.

[36] C. Wu, Y. Zhang, and B. O. Guan, “Simultaneous measurement of temperature and hydrostatic pressure using bragg gratings in standard and grapefruit microstructured fibers,” *IEEE Sens J*, vol. 11, no. 2, 2011, doi: 10.1109/JSEN.2010.2068045.

[37] F. Esposito, A. Srivastava, A. Iadicicco, and S. Campopiano, “Multi-parameter sensor based on single Long Period Grating in Panda fiber for the simultaneous measurement of SRI, temperature and strain,” *Opt Laser Technol*, vol. 113, 2019, doi: 10.1016/j.optlastec.2018.12.022.

[38] X. Jin, J. S. Sirkis, and J.-K. Chung, “Optical fiber sensor for simultaneous measurement of strain and temperature,” in *Smart Structures and Materials 1997: Smart Sensing, Processing, and Instrumentation*, 1997, vol. 3042. doi: 10.1117/12.275764.

[39] M. M. Ali, M. R. Islam, K. S. Lim, D. S. Gunawardena, H. Z. Yang, and H. Ahmad, “PCF-Cavity FBG Fabry-Perot Resonator for Simultaneous Measurement of Pressure and Temperature,” *IEEE Sens J*, vol. 15, no. 12, 2015, doi: 10.1109/JSEN.2015.2468065.

[40] T. Zhang *et al.*, “Constructed fiber-optic FPI-based multi-parameters sensor for simultaneous measurement of pressure and temperature, refractive index and temperature,” *Optical Fiber Technology*, vol. 49, 2019, doi: 10.1016/j.yofte.2019.02.007.

[41] T. Liu, Y. Chen, Q. Han, F. Liu, and Y. Yao, “Sensor based on macrobent fiber Bragg grating structure for simultaneous measurement of refractive index and temperature,” *Appl Opt*, vol. 55, no. 4, 2016, doi: 10.1364/ao.55.000791.

[42] R. Oliveira, J. H. Osório, S. Aristilde, L. Bilro, R. N. Nogueira, and C. M. B. Cordeiro, “Simultaneous measurement of strain, temperature and refractive index based on multimode interference, fiber tapering and fiber Bragg gratings,” *Meas Sci Technol*, vol. 27, no. 7, 2016, doi: 10.1088/0957-0233/27/7/075107.

[43] J. Yu, S. Xu, Y. Jiang, H. Chen, and W. Feng, “Multi-parameter sensor based on the fiber Bragg grating combined with triangular-lattice four-core fiber,” *Optik (Stuttg)*, vol. 208, 2020, doi: 10.1016/j.ijleo.2019.164094.

[44] X. Fu *et al.*, “A Multi-parameter Sensor Based on Dumbbell-shaped Double-cladding Fiber Structure Cascaded Long Period Fiber Grating,” *IEEE Sens J*, Jul. 2022, doi: 10.1109/JSEN.2022.3181677.

[45] C. Li *et al.*, “Simultaneous measurement of refractive index, strain, and temperature based on a four-core fiber combined with a fiber Bragg grating,” *Opt Laser Technol*, vol. 90, 2017, doi: 10.1016/j.optlastec.2016.11.019.

[46] R. Gao, D. Lu, J. Cheng, and Z. M. Qi, “In-Fiber Double-Layered Resonator for High-Sensitive Strain Sensing,” *IEEE Photonics Technology Letters*, vol. 29, no. 11, 2017, doi: 10.1109/LPT.2017.2693218.

[47] M. Hou *et al.*, “Antiresonant reflecting guidance mechanism in hollow-core fiber for gas pressure sensing,” *Opt Express*, vol. 24, no. 24, 2016, doi: 10.1364/oe.24.027890.

[48] H. Gao *et al.*, “Antiresonant mechanism based self-temperature-calibrated fiber optic Fabry–Perot gas pressure sensors,” *Opt Express*, vol. 27, no. 16, 2019, doi: 10.1364/oe.27.022181.

[49] H. Cheng, S. Wu, Q. Wang, S. Wang, and P. Lu, “In-Line Hybrid Fiber Sensor for Curvature and Temperature Measurement,” *IEEE Photonics J*, vol. 11, no. 6, 2019, doi: 10.1109/JPHOT.2019.2944988.

[50] S. Wang *et al.*, “Curvature and Temperature Sensor Based on Anti-Resonant Effect Combined with Multimode Interference,” *IEEE Photonics Technology Letters*, vol. 33, no. 3, 2021, doi: 10.1109/LPT.2020.3048988.

[51] C. He *et al.*, “Simultaneous measurement of strain and temperature using Fabry–Pérot interferometry and antiresonant mechanism in a hollow-core fiber,” *Chinese Optics Letters*, vol. 19, no. 4, 2021, doi: 10.3788/col202119.041201.

[52] Y. B. Yang, D. N. Wang, B. Xu, and Z. K. Wang, “Optical fiber tip interferometer gas pressure sensor based on anti-resonant reflecting guidance mechanism,” *Optical Fiber Technology*, vol. 42, 2018, doi: 10.1016/j.yofte.2018.02.013.

[53] D. Pereira, J. Bierlich, J. Kobelke, and M. S. Ferreira, “Double antiresonance fiber sensor for the simultaneous measurement of curvature and temperature,” *Sensors*, vol. 21, no. 23, 2021, doi: 10.3390/s21237778.

[54] D. Pereira, J. Bierlich, J. Kobelke, and M. S. Ferreira, “Hybrid sensor based on a hollow square core fiber for temperature independent refractive index detection,” *Opt Express*, vol. 30, no. 11, 2022, doi: 10.1364/oe.456529.

[55] D. Pereira, J. Bierlich, J. Kobelke, and M. S. Ferreira, “Simultaneous measurement of strain, curvature, and temperature using a hollow square core fiber,” *Opt Laser Technol*, vol. 156, p. 108540, Dec. 2022, doi: 10.1016/j.optlastec.2022.108540.

[56] T. Nan *et al.*, “Three-parameter measurement optical fiber sensor based on a hybrid structure,” *Appl Opt*, vol. 59, no. 27, 2020, doi: 10.1364/ao.401652.

[57] J. L. Archambault, R. J. Black, S. Lacroix, and J. Bures, “Loss Calculations for Antiresonant Waveguides,” *Journal of Lightwave Technology*, vol. 11, no. 3, 1993, doi: 10.1109/50.219574.

[58] W. Sun *et al.*, “Comparative Study on Transmission Mechanisms in a SMF-Capillary-SMF Structure,” *Journal of Lightwave Technology*, vol. 38, no. 15, 2020, doi: 10.1109/JLT.2020.2983910.

[59] I. H. Malitson, “Interspecimen Comparison of the Refractive Index of Fused Silica,” *J Opt Soc Am*, vol. 55, no. 10, 1965.

[60] M. Deng, C. P. Tang, T. Zhu, and Y. J. Rao, “PCF-based Fabry-Pérot interferometric sensor for strain measurement at high temperatures,” *IEEE Photonics Technology Letters*, vol. 23, no. 11, 2011, doi: 10.1109/LPT.2011.2124452.

[61] N. M. Litchinitser, A. K. Abeeluck, C. Headley, and B. J. Eggleton, “Antiresonant reflecting photonic crystal optical waveguides,” *Opt Lett*, vol. 27, no. 18, 2002, doi: 10.1364/ol.27.001592.

[62] S. Liu, Y. Wang, M. Hou, J. Guo, Z. Li, and P. Lu, “Anti-resonant reflecting guidance in alcohol-filled hollow core photonic crystal fiber for sensing applications,” *Opt Express*, vol. 21, no. 25, 2013, doi: 10.1364/oe.21.031690.

[63] S. Liu, Y. Ji, L. Cui, W. Sun, J. Yang, and H. Li, “Humidity-insensitive temperature sensor based on a quartz capillary anti-resonant reflection optical waveguide,” *Opt Express*, vol. 25, no. 16, 2017, doi: 10.1364/oe.25.018929.

[64] “Corning SMF-28 Optical Fiber Product Information,” 2002.

[65] B. Xu, Y. Liu, D. Wang, D. Jia, and C. Jiang, “Optical fiber fabry-pérot interferometer based on an air cavity for gas pressure sensing,” *IEEE Photonics J*, vol. 9, no. 2, 2017

[66] L. Shao, Z. Liu, J. Hu, D. Gunawardena, and H. Y. Tam, “Optofluidics in microstructured optical fibers,” *Micromachines*, vol. 9, no. 4. 2018. doi: 10.3390/mi9040145.

[67] Y. Zheng *et al.*, “Fiber optic Fabry-Perot optofluidic sensor with a focused ion beam ablated microslot for fast refractive index and magnetic field measurement,” *IEEE Journal of Selected Topics in Quantum Electronics*, vol. 23, no. 2, 2017, doi: 10.1109/JSTQE.2017.2649462.

[68] K. Sloyan, H. Melkonyan, H. Apostoleris, M. S. Dahlem, M. Chiesa, and A. al Ghaferi, “A review of focused ion beam applications in optical fibers,” *Nanotechnology*, vol. 32, no. 47. 2021. doi: 10.1088/1361-6528/ac1d75.

[69] V. A. Drebushchak, “The Peltier effect,” *J Therm Anal Calorim*, vol. 91, no. 1, 2008, doi: 10.1007/s10973-007-8336-9.

[70] C. Zhu, R. E. Gerald, and J. Huang, “A Dual-Parameter Internally Calibrated Fabry-Perot Microcavity Sensor,” *IEEE Sens J*, vol. 20, no. 5, 2020, doi: 10.1109/JSEN.2019.2954042.

[71] R. Tong, Y. Zhao, M. Chen, X. Hu, and Y. Yang, “Simultaneous measurement of RH and temperature based on FBG and balloon-like sensing structure with inner embedded up-tapered MZI,” *Measurement (Lond)*, vol. 146, 2019, doi: 10.1016/j.measurement.2019.06.018.

[72] Y. Wu, F. Meng, H. Li, G. Yan, and L. Zhu, “Simultaneous measurement of micro-displacement and temperature based on balloon-like interferometer and fiber Bragg grating,” *Optik (Stuttg)*, vol. 183, 2019, doi: 10.1016/j.ijleo.2019.03.009.

[73] L. Cai, X. Ai, and Y. Zhao, “A displacement sensor based on balloon-like optical fiber structure,” *Sens Actuators A Phys*, vol. 338, 2022, doi: 10.1016/j.sna.2022.113469.

[74] X. Ding, T. Jin, and R. Zhang, “Balloon-like angle and micro-displacement sensor based on bent single-mode fiber,” *Optical Fiber Technology*, vol. 68, 2022, doi: 10.1016/j.yofte.2021.102787.

[75] K. Tian *et al.*, “Simultaneous measurement of displacement and temperature based on two cascaded balloon-like bent fibre structures,” *Optical Fiber Technology*, vol. 58, 2020, doi: 10.1016/j.yofte.2020.102277.

[76] J. Zheng *et al.*, “An Optical Sensor Designed from Cascaded Anti-Resonant Reflection Waveguide and Fiber Ring-Shaped Structure for Simultaneous Measurement of Refractive Index and Temperature,” *IEEE Photonics J*, vol. 14, no. 1, 2022, doi: 10.1109/JPHOT.2022.3144156.

[77] J. D. C. Jones, “Review of Fibre Sensor Techniques for Temperature-Strain Discrimination,” in *Optics InfoBase Conference Papers*, 1997. doi: 10.1364/ofs.1997.otuc1.

[78] Y. Chen, Q. Han, T. Liu, F. Liu, and Y. Yunzhi, “Simultaneous Measurement of Refractive Index and Temperature Using a Cascaded FBG/Droplet-Like Fiber Structure,” *IEEE Sens J*, vol. 15, no. 11, 2015, doi: 10.1109/JSEN.2015.2450361.

[79] K. Tian, G. Farrell, W. Yang, X. Wang, E. Lewis, and P. Wang, “Simultaneous Measurement of Displacement and Temperature Based on a Balloon-Shaped Bent SMF Structure Incorporating an LPG,” *Journal of Lightwave Technology*, vol. 36, no. 20, 2018, doi: 10.1109/JLT.2018.2866488.

[80] C. Li *et al.*, “A knotted shape core cladding optical fiber interferometer for simultaneous measurement of displacement and temperature,” *Photonics Nanostruct*, vol. 39, 2020, doi: 10.1016/j.photonics.2020.100778.

[81] J. P. Santos, J. Bierlich, J. Kobelke, and M. S. Ferreira, “Simultaneous measurement of displacement and temperature using a balloon-like hybrid fiber sensor,” *Opt Lett*, vol. 47, no. 15, p. 3708, Aug. 2022, doi: 10.1364/ol.465403.

[82] D. Liu *et al.*, “Hollow Core Fiber Based Interferometer for High-Temperature (1000 °C) Measurement,” *Journal of Lightwave Technology*, vol. 36, no. 9, 2018, doi: 10.1109/JLT.2017.2784544.